DRAFT VERSION JULY 18, 2014
Preprint typeset using LaTeX style emulateapj v. 04/17/13

arXiv:1406.2314v2 [astro-ph.GA] 16 Jul 2014

HALO MASS DEPENDENCE OF H I AND O VI ABSORPTION: EVIDENCE FOR DIFFERENTIAL KINEMATICS

NIGEL L. MATHES[1], CHRISTOPHER W. CHURCHILL[1], GLENN G. KACPRZAK[2,3], NIKOLE M. NIELSEN[1],
SEBASTIAN TRUJILLO-GOMEZ[1], JANE CHARLTON[4], AND SOWGAT MUZAHID[4]

Draft version July 18, 2014

ABSTRACT

We studied a sample of 14 galaxies ($0.1 < z < 0.7$) using *HST*/WFPC2 imaging and high-resolution *HST*/COS or *HST*/STIS quasar spectroscopy of Lyα, Lyβ, and O VI $\lambda\lambda$1031, 1037 absorption. The galaxies, having $10.8 \leq \log(M_{\rm h}/M_{\odot}) \leq 12.2$, lie within $D = 300$ kpc of quasar sightlines, probing out to $D/R_{\rm vir} = 3$. When the full range of $M_{\rm h}$ and $D/R_{\rm vir}$ of the sample are examined, $\sim$40% of the H I absorbing clouds can be inferred to be escaping their host halo. The fraction of bound clouds decreases as $D/R_{\rm vir}$ increases such that the escaping fraction is $\sim$15% for $D/R_{\rm vir} < 1$, $\sim$45% for $1 \leq D/R_{\rm vir} < 2$, and $\sim$90% for $2 \leq D/R_{\rm vir} < 3$. Adopting the median mass $\log M_{\rm h}/M_{\odot} = 11.5$ to divide the sample into "higher" and "lower" mass galaxies, we find mass dependency for the hot CGM kinematics. To our survey limits, O VI absorption is found in only $\sim$40% of the H I clouds in and around lower mass halos as compared to $\sim$85% around higher mass halos. For $D/R_{\rm vir} < 1$, lower mass halos have an escape fraction of $\sim$65%, whereas higher mass halos have an escape fraction of $\sim$5%. For $1 \leq D/R_{\rm vir} < 2$, the escape fractions are $\sim$55% and $\sim$35% for lower mass and higher mass halos, respectively. For $2 \leq D/R_{\rm vir} < 3$, the escape fraction for lower mass halos is $\sim$90%. We show that it is highly likely that the absorbing clouds reside within $4R_{\rm vir}$ of their host galaxies and that the kinematics are dominated by outflows. Our finding of "differential kinematics" is consistent with the scenario of "differential wind recycling" proposed by Oppenheimer et al. We discuss the implications for galaxy evolution, the stellar to halo mass function, and the mass metallicity relationship of galaxies.

Keywords: galaxies: halos — quasars: absorption lines

1. INTRODUCTION

Characterizing the baryonic gas processes within and surrounding galaxies is central to understanding their formation and evolution. Quantifying the spatial extent, kinematics, and, in particular, the recycling and/or escape fraction of circumgalactic gas are of primary importance in that they place direct observational constraints on simulations of galaxies and provide insights into the workings of galaxy evolution.

High-resolution spectroscopy of quasars, which provide a background luminous source, and high-resolution imaging of the foreground galaxies provides the data necessary for examining the kinematics of galactic gas and its geometric distribution with respect to the galaxy projected orientation.

In general, the gas structures in and around galaxies can be divided into three broad categories: the interstellar medium (ISM), the circumgalactic medium (CGM), and the intergalactic medium (IGM). The CGM, being the gas reservoir that interfaces with the star-forming ISM, outflowing stellar-driven winds, and the accreting IGM, may contain up to 50% of the baryonic mass bound to galaxies (Tumlinson et al. 2011) and account for up to 50% of the baryons unaccounted for in galaxy dark matter halos (Werk et al. 2014). As such, the CGM may play the most critical role in governing the properties of galaxies (e.g., Oppenheimer et al. 2010; Churchill et al. 2013b), including regulatory physics leading to the observed stellar mass function (e.g., Behroozi et al. 2013) and the stellar mass-ISM metallicity relationship (e.g., Tremonti et al. 2004).

The physical extent of the CGM and the transition zone between the CGM and IGM are currently open questions. Studies by Steidel et al. (2010), Prochaska et al. (2011), and Rudie et al. (2012) indicate a transition from the CGM to the IGM at $\log N({\rm H\,I}) \simeq 14$ and a projected distance of $\sim$300 kpc from galaxies at $z \sim 2.5$. At this redshift, $\log N({\rm H\,I}) \simeq 14$ corresponds to an overdensity of $\log \rho_{\rm H}/\bar{\rho}_{\rm H} \simeq 0.5$, whereas at $z \simeq 0$, this overdensity would suggest a CGM/IGM transition at $\log N({\rm H\,I}) \simeq 13$ (see Davé et al. 1999). Indeed, Ford et al. (2013) show that, in the over-dense regions hosting galaxies, the extent of the H I at fixed column density increases with virial mass, suggesting that a single fiducial physical size for the CGM may not apply across the entire mass range of galaxies; it may be more appropriate to scale CGM properties relative to the virial radius (e.g., Churchill et al. 2013a,b)

Cosmological hydrodynamic simulations indicate that the virial mass may dictate the temperature history, density, and mode of IGM accretion (Birnboim & Dekel 2003; Kereš et al. 2005; Dekel & Birnboim 2006; Kereš et al. 2009; van de Voort et al. 2011; Fumagalli et al. 2011; van de Voort & Schaye 2012). The recycling timescale of wind material back into the ISM may depend upon galaxy virial mass according to what Oppenheimer et al. (2010) call "differential wind recycling". Their simulations suggest that the recycling time of wind material through the CGM could be shorter for higher mass halos, and possibly longer than the Hubble time for the lowest mass halos, and that this behavior may be key for understanding the galaxy stellar mass function in the low mass range. As deduced from the simulations, differential wind recycling is primarily due to greater hydrodynamic (not gravitational) deceleration of wind material in higher mass halos due to their being embedded in denser gas environments, leading to diminished recycling times (also see Oppenheimer & Davé 2008).

As probed by Mg II absorption (see Nielsen et al. 2013a,b,

[1] New Mexico State University, Las Cruces, NM 88003
[2] Swinburne University of Technology, Victoria 3122, Australia
[3] Australian Research Council Super Science Fellow
[4] The Pennsylvania State University, University Park, PA 16802

and references therein), the observed projected absorption profile, covering fraction, and physical extent of the cool gas component of the CGM combine to suggest that the cool/warm CGM exhibits a self-similar radial behavior with virial mass (Churchill et al. 2013a,b). Mg II absorption properties behave self-similarly with $D/R_{\rm vir}$, the projected distance of the absorption from the galaxy relative to the virial radius. Stocke et al. (2013) also report behavior that can be interpreted as self-similarity in that, once impact parameter is scaled by $R_{\rm vir}$, the cool/warm CGM gas properties show little-to-no variation as a function of projected distance, gas kinematics, and galaxy luminosity (however, see Werk et al. 2014, who report weak anti-correlations in the cloud hydrogen number densities and ionization parameters). If virial mass influences the global physics of the CGM, then the CGM/IGM boundary and ISM/stellar formation physics of galaxies may fundamentally be related to the dark matter overdensity profile of halos within the virial radius.

Simulations of starbursts predict that outflowing gas will preferentially escape along the galaxy minor axis (e.g., Strickland et al. 2004). Infalling gas is predicted to preferentially accrete in the galactic plane and kinematically trace galaxy rotation (e.g., Stewart et al. 2011), consistent with the observations of Steidel et al. (2002) and Kacprzak et al. (2010). Consistent with these predictions, Mg II absorption is most commonly found along the projected minor and major axes of galaxies (Bouché et al. 2012; Kacprzak et al. 2012a). Bordoloi et al. (2011) report that, on average, larger Mg II equivalent widths are found along the projected minor axis as compared to the projected major axis. The distribution of H I, traced using Lyα absorption, appears to be more uniform with respect to the galaxy projected axis (e.g., Stocke et al. 2013).

The kinematics of CGM/IGM absorption with respect to host galaxy escape velocity places direct observational constraints on the influence of hydrodynamic and/or gravitational deceleration of CGM gas and provides insights into the plausibility of a mass dependent wind recycling scenario. For $D < 150$ kpc (corresponding to $D/R_{\rm vir} < 1$), Tumlinson et al. (2011, 2013) find that, in moderate to high mass halos with $\log(M_{\rm h}/M_{\odot}) > 11.3$, CGM gas is predominantly bound. Stocke et al. (2013) find that the majority of the CGM within the projected virial radius also appears bound, but outside of the projected virial radius, velocities can exceed the escape velocity.

Simulations, such as those by Kereš et al. (2005) and by van de Voort & Schaye (2012), predict that more massive halos have higher hot gas mass fractions. The metal-enriched hot phase of the CGM, which can be traced by O VI absorption, may be a reservoir of a significant baryonic mass (Tumlinson et al. 2011). The hot phase may serve as a "coronal" hydrostatic region surrounding galaxies that strongly governs the formation and destruction of the cool/warm CGM "clouds" (Mo & Miralda-Escude 1996; Maller & Bullock 2004; Dekel & Birnboim 2006). On the other hand, gas traced by O VI absorption may arise in multiphase gas structures (Prochaska et al. 2004; Cooksey et al. 2008).

Although O VI absorbing gas has been extensively studied in the Galactic, extragalactic, and IGM environments (Savage et al. 2002, 2003; Richter et al. 2004; Sembach et al. 2004; Lehner et al. 2006; Danforth & Shull 2008; Tripp et al. 2008; Thom et al. 2011; Tumlinson et al. 2011; Muzahid 2014), the potential important role of CGM gas beckons further exploration of O VI absorption around galaxies in order to address basic questions such as: what is the physical extent of O VI absorbing gas around galaxies, and where is the CGM/IGM transition region of the hot phase? Can a CGM/IGM transition region, or boundary, be observationally discerned? Is the transition region halo mass dependent? Are there trends in the hot phase with respect to a galaxy's virial radius? Does the hot phase have a preferred geometrical distribution around galaxies, similar or dissimilar to what is seen for the cold/warm phase? Is there kinematic evidence for the differential wind recycling scenario?

In order to address these questions, we examine the kinematics and spatial distribution of H I and O VI column densities in the CGM/IGM and their absorption kinematics for a small sample of galaxies. This paper is structured as follows: In Section 2 we discuss the sample selection, the data, and data analysis. In Section 3, we examine the spatial extent and geometry of the H I and O VI absorbing gas. In Section 4, we compare the H I and O VI kinematics and examine the spatial and virial mass dependence of the CGM with respect to halo escape velocity. In Section 5, we discuss our findings and in Section 6 we summarize our results and discussion. Throughout, we adopt a ΛCDM cosmological model with $h = 0.7$, where $h = H_0/100$ km s^{-1} Mpc^{-1}, with $\Omega_m = 0.3$ and $\Omega_\Lambda = 0.7$.

2. SAMPLE SELECTION, DATA, AND ANALYSIS

2.1. *Sample Selection*

We have assembled a sample of 14 galaxies in the fields of UV bright quasars with high resolution *HST* imaging and ultraviolet spectra. We impose four primary criteria for the galaxy sample: (1) each galaxy must be intervening to a background quasar within a projected distance of 300 kpc from the line of sight and must have a spectroscopic redshift measurement, (2) each galaxy must be imaged with the *Hubble Space Telescope* (*HST*), (3) a *HST*/COS and/or STIS spectrum of the background quasar is available that, at a minimum, covers the redshifted Lyα, Lyβ, and O VI $\lambda\lambda$1031, 1037 transitions within $\pm$1000 km s^{-1} of the associated foreground galaxy redshift, and (4) the foreground galaxy must not reside in a group or cluster environment to the extent that the data provides such information.

The 300 kpc projected distance allows us to study the CGM out to the extent probed by Steidel et al. (2010), Prochaska et al. (2011), and Rudie et al. (2012) and to extend beyond the 150 kpc range probed by Tumlinson et al. (2011, 2013). The *HST*/WFPC2 images provide the spatial information required to measure galaxy morphological parameters and determine galaxy orientations relative to the quasar line of sight. The *HST*/COS and/or STIS spectroscopy allows Voigt profile decomposition of the Lyα, Lyβ, and O VI $\lambda\lambda$1031, 1037 absorption profiles, providing individual "cloud" column densities and kinematics.

By selecting isolated field galaxies, we aim to study the CGM independent of galaxy environment. In a given quasar field, we first require that no other galaxy is identified within $\pm$1000 km s^{-1} (based upon redshift). If other galaxies exist in the field within this velocity window, we then require the galaxies lie farther than a projected distance of 600 kpc from the quasar line of sight.

The quasar fields from which the galaxy sample is drawn were surveyed by Ellingson & Yee (1994), Lanzetta et al. (1995), Le Brun et al. (1996), Chen et al. (2001), and

Table 1
Journal of Observations

(1) Quasar	(2) Instrument	(3) Filter/Grating	(4) Exp. Time [s]	(5) PID
Q0405–123	*HST*/WFPC2	F702W	2400	5949
	HST/COS	G130M+G160M	20,749	11541
Q0454–2203	*HST*/WFPC2	F702W	1200	5098
	HST/COS	G160M	2778	12252
	HST/COS	G160M	1849	12466
	HST/COS	G185M	74,410	12536
Q1001+2910	*HST*/WFPC2	F702W	2400	5949
	HST/COS	G130M+G160M	12,988	12,038
Q1136–1334	*HST*/WFPC2	F702W	2100	6919
	HST/COS	G130M	7751	12275
Q1216+0655	*HST*/WFPC2	F702W	2100	6619
	HST/COS	G130M+G160M	10,702	12025
Q1259+5920	*HST*/WFPC2	F702W	2100	6919
	HST/WFPC2	F702W	2100	6919
	HST/COS	G130M+G160M	20,383	11541
Q1317+2743	*HST*/WFPC2	F702W	4700	5984
	HST/COS	G160M+G185M	22,971	11667
Q1704+6048	*HST*/WFPC2	F702W	2400	5949
	HST/STIS	E140M	22,155	8015

Johnson et al. (2013). We note that the fields have been studied for different science goals employing different facilities to varying degrees of completeness. A detailed discussion of the application of the galaxy selection criteria for each field is presented in Appendix A. Here, we briefly summarize the surveys. The galaxies observed by Ellingson & Yee (1994) have redshifts $0.3 < z < 0.6$ and are intervening to radio-selected quasars. The galaxies surveyed by Lanzetta et al. (1995), Le Brun et al. (1996), and Chen et al. (2001) have redshifts $0.05 < z < 0.8$ are selected on the basis that *HST*/FOS spectra of the quasar had been obtained for the *HST* Key Project (cf., Bahcall et al. 1993).

The resulting redshift range of our galaxy sample is determined exclusively by the UV spectral coverage of the *HST*/COS and STIS observations and not by any *a priori* redshift cuts. Using the above four selection criteria, we compiled a sample of 14 galaxies spanning the redshift range of $0.12 \leq z \leq 0.67$ with impact parameters from $60 \leq D \leq 290$ kpc.

In Table 1, we list the observational data employed for the sample galaxies. Column (1) lists the quasar field [B1950 designation]. Column (2) lists the imaging and spectroscopic instruments. Column (3) lists the imaging filter and the COS or STIS grating. Columns (4) and (5) list the exposure time and the program ID, respectively.

2.2. *Galaxy Imaging and Photometric Properties*

All *HST*/WFPC2 images were obtained using the F702W band. We adopted the reduced and calibrated images from the WFPC-2 Associations Science Products Pipeline (WASPP[5]).

The galaxy apparent Vega magnitudes, $m_{\rm F702W}$, were determined using 1.5 σ isophotes from Source Extractor (Bertin & Arnouts 1996). From the galaxy centroids, we compute the galaxy offset from the quasar (arcsec) and the galaxy-quasar sightline impact parameter (kpc). We computed AB r-band absolute magnitudes, M_r, by k-correcting the observed F702W magnitudes following the method of Nielsen et al. (2013b). To determine galaxy virial masses, $M_{\rm h}$, we performed halo abundance matching (e.g., Behroozi et al. 2010; Trujillo-Gomez et al. 2011) following the method of Churchill et al. (2013b), in which we match the distribution of the maximum circular velocity of halos in the Bolshoi N-body cosmological simulation of Klypin et al. (2011) to the COMBO-17 r-band luminosity function of Wolf et al. (2003). Galaxy virial radii are then computed from $M_{\rm h}$ using the relation of Bryan & Norman (1998). Uncertainties in the viral masses and virial radii, which are on the order 10%, originate from the scatter in the virial mass circular velocity distribution function (see Churchill et al. 2013b, for details).

Quantified galaxy morphological parameters were measured using GIM2D (Simard et al. 2002) following the methods of Kacprzak et al. (2011). GIM2D models the two-dimensional brightness profiles of the galaxies and computes the inclination, i, and the position angle, Φ, on the sky. We adopt the formalism that $i = 0^\circ$ is face-on and $i = 90^\circ$ is edge-on. We translate the position angle to an "azimuthal angle" defined such that for $\Phi = 0^\circ$ the quasar sightline lies along the projected major axis, and for $\Phi = 90^\circ$ it lies along the galaxy projected minor axis.

In Table 2, columns (1) and (2) list the quasar field and the galaxy spectroscopic redshift. Columns (3)–(5) list the galaxy offsets relative to the quasar and the galaxy impact parameter, respectively. Columns (6) and (7) list the galaxy *HST*/WFPC2 F702W apparent magnitude (Vega) and the r-band absolute magnitude (AB). Columns (8) and (9) list the virial mass and virial radius of the galaxy. Columns (10) and (11) list the galaxy azimuthal angle and inclination.

The galaxy WFPC/F702W apparent magnitudes range from $22.6 \geq m_{\rm F702W} \geq 17.8$. Absolute r-band magnitudes range from $-15.5 \geq M_r \geq -20.2$. The range of galaxy inclinations and azimuthal angles are $18^\circ \leq i \leq 85^\circ$ and $6^\circ \leq \Phi \leq 87^\circ$, respectively. The virial masses range from $10.8 \leq \log(M_{\rm h}/M_\odot) \leq 12.2$, with virial radii between $70 \leq R_{\rm vir} \leq 225$ kpc. The median virial mass is $\log(M_{\rm h}/M_\odot) = 11.5$.

2.3. *Quasar Spectra and Absorption Properties*

The *HST*/COS spectra were reduced and flux calibrated using the CalCOS pipeline (V2.11). Vacuum and heliocentric corrections, dispersion alignment, and co-addition of individual exposures were performed using software developed by the COS team[6] (also see Narayanan et al. 2011).

Reduction and calibration of the E140M *HST*/STIS spectrum (for Q1704+6048 using the $0.2'' \times 0.2''$ slit) was performed using the standard STIS pipeline (Brown et al. 2002). Further details are discussed in Narayanan et al. (2005). Continuum fitting for both the *HST*/COS and *HST*/STIS data sets was conducted using the interactive SFIT task in IRAF[7] following the methods described in Sembach & Savage (1992). We then refined higher order continuum fits using our own code, FITTER (Churchill et al. 2000).

[5] http://archive.stsci.edu/hst/wfpc2/pipeline.html

[6] http://casa.colorado.edu/∼danforth/science/cos/costools.html

[7] IRAF is distributed by the National Optical t Astronomy Observatory, which is operated by the Association of Universities for Research in Astronomy (AURA) under cooperative agreement with the National Science Foundation.

Table 2
Galaxy Properties

(1) Quasar	(2) z_{gal}	(3) $\Delta\alpha$ [arcsec]	(4) $\Delta\delta$ [arcsec]	(5) D [kpc]	(6) m_{F702W} [Vega]	(7) M_r [AB]	(8) $\log(M_h)$ [$M_\odot$]	(9) R_{vir} [kpc]	(10) Φ [deg]	(11) i [deg]
Q0405–123	0.1534	–66.2	–30.9	196	18.19	–19.21	$11.8^{+0.4}_{-0.2}$	152^{+56}_{-23}	$26.3^{+0.9}_{-1.0}$	$49.5^{+0.5}_{-0.7}$
Q0405–123	0.2978	31.9	–47.9	258	19.23	–19.86	$12.2^{+0.2}_{-0.2}$	224^{+41}_{-28}	$22.4^{+1.1}_{-1.3}$	$62.1^{+1.9}_{-2.8}$
Q0405–123	0.4100	2.6	–23.2	292	22.58	–17.37	$11.2^{+0.5}_{-0.2}$	106^{+52}_{-15}	$44.4^{+28.0}_{-46.0}$	$60.7^{+24.3}_{-37.6}$
Q0454–2203	0.3818	0.3	–19.7	103	20.41	–19.35	$12.0^{+0.3}_{-0.2}$	194^{+46}_{-26}	$63.8^{+4.3}_{-2.7}$	$57.1^{+19.9}_{-2.4}$
Q1001+2910	0.1380	–3.4	–23.1	57	21.65	–15.49	$10.8^{+0.7}_{-0.2}$	73^{+48}_{-11}	$12.4^{+2.4}_{-2.9}$	$79.1^{+2.2}_{-2.1}$
Q1001+2910	0.2143	13.4	–61.8	222	21.64	–16.59	$11.2^{+0.6}_{-0.2}$	98^{+55}_{-15}	$14.2^{+44.2}_{-42.7}$	$18.1^{+20.5}_{-18.1}$
Q1136–1334	0.1755	–3.2	55.7	166	21.30	–16.43	$11.0^{+0.7}_{-0.2}$	86^{+56}_{-13}	$44.3^{+4.5}_{-4.9}$	$84.8^{+0.2}_{-3.4}$
Q1136–1334	0.2044	10.8	–25.5	93	19.69	–18.42	$11.7^{+0.4}_{-0.2}$	146^{+53}_{-21}	$5.8^{+0.4}_{-0.5}$	$83.4^{+0.4}_{-0.5}$
Q1216+0655	0.1242	37.2	–18.8	95	17.78	–19.11	$11.7^{+0.4}_{-0.2}$	146^{+56}_{-22}	$68.0^{+0.4}_{-0.5}$	$85.0^{+0.0}_{-0.0}$
Q1259+5920	0.1967	27.0	–31.3	135	20.55	–17.46	$11.2^{+0.6}_{-0.2}$	103^{+62}_{-16}	$39.7^{+2.8}_{-2.2}$	$80.7^{+4.3}_{-3.2}$
Q1259+5920	0.2412	–23.4	68.5	280	19.58	–18.96	$11.9^{+0.3}_{-0.2}$	169^{+50}_{-24}	$42.5^{+4.0}_{-3.7}$	$71.9^{+1.5}_{-2.9}$
Q1317+2743	0.6610	10.2	–7.4	103	21.34	–20.15	$12.1^{+0.2}_{-0.2}$	224^{+35}_{-25}	$87.0^{+1.0}_{-1.0}$	$65.8^{+1.2}_{-1.2}$
Q1704+6048	0.1877	72.9	5.9	231	18.05	–19.85	$12.0^{+0.3}_{-0.2}$	190^{+50}_{-27}	$47.1^{+0.7}_{-0.8}$	$60.9^{+0.6}_{-0.6}$
Q1704+6048	0.3380	–31.3	–9.4	159	21.26	–18.16	$11.6^{+0.4}_{-0.2}$	140^{+53}_{-21}	$53.8^{+3.6}_{-2.9}$	$53.1^{+7.1}_{-15.3}$

Table 3
Absorption Properties

(1) Quasar	(2) z_{gal}	(3) z_{abs}	(4) W_r(Lyα) [Å]	(5) W_r(Lyβ) [Å]	(6) W_r(O VI) [Å]	(7) $\log N$(H I) [cm^{-2}]	(8) $\log N$(O VI) [cm^{-2}]	(9)[a] $v^{(-)}$ [km s^{-1}]	(10)[a] $v^{(+)}$ [km s^{-1}]
Q0405–123	0.1534	0.1530	0.547 ± 0.014	0.112 ± 0.011	0.019 ± 0.004	14.13 ± 0.03	13.40 ± 0.07	–575	212
Q0405–123	0.2978	0.2977	0.343 ± 0.014	0.061 ± 0.007	0.036 ± 0.006	14.00 ± 0.06	13.50 ± 0.23	–194	87
Q0405–123	0.4100	0.4059	0.966 ± 0.021	0.437 ± 0.011	0.048 ± 0.007	14.98 ± 0.95	13.76 ± 0.11	–1024	–48
Q0454–2203	0.3818	0.3817	0.609 ± 0.131	0.368 ± 0.052	0.255 ± 0.059	14.63 ± 0.25	14.41 ± 0.65	–230	248
Q1001+2910	0.1380	0.1375	0.776 ± 0.018	0.322 ± 0.017	0.084 ± 0.010	14.91 ± 0.06	14.03 ± 0.03	–768	12
Q1001+2910	0.2143	0.2128	0.736 ± 0.055	0.285 ± 0.037	0.073 ± 0.014	14.33 ± 0.33	14.00 ± 0.13	–556	50
Q1136–1334	0.1755	0.1749	0.661 ± 0.050	< 0.227	< 0.356	14.35 ± 0.10	< 13.50	–347	49
Q1136–1334	0.2044	0.2044	1.383 ± 0.173	1.395 ± 0.033	0.147 ± 0.033	15.94 ± 0.85	14.29 ± 0.16	–456	293
Q1216+0655	0.1242	0.1242	1.376 ± 0.022	0.660 ± 0.063	0.447 ± 0.058	15.26 ± 0.38	14.72 ± 0.26	–254	268
Q1259+5920	0.1967	0.1963	0.442 ± 0.024	< 0.123	0.040 ± 0.004	13.99 ± 0.15	13.73 ± 0.24	–307	441
Q1259+5920	0.2412	0.2412	0.049 ± 0.015	< 0.042	< 0.088	13.06 ± 0.07	< 11.84	–100	99
Q1317+2743	0.6610	0.6605	1.542 ± 0.091	0.905 ± 0.030	0.258 ± 0.043	18.53 ± 0.87	14.51 ± 0.08	–514	344
Q1704+6048	0.1877	0.1875	0.387 ± 0.011	0.044 ± 0.007	0.053 ± 0.013	14.08 ± 0.01	13.72 ± 0.07	–133	80
Q1704+6048	0.3380	0.3380	< 0.086	< 0.049	< 0.050	< 12.00	< 12.00	–100	99

[a] The velocities correspond to the Lyα absorption.

We searched the quasar spectra for Lyα, Lyβ, and O VI $\lambda\lambda$1031, 1037 absorption within $\pm$1000 km s^{-1} of the identified galaxy redshift. We adopt the objective detection methods of Schneider et al. (1993) using the 5 σ uncertainty in the equivalent width spectrum. Once an absorption feature is identified, we use the methods of Churchill et al. (1999) and Churchill & Vogt (2001) to measure the velocity extremes of the absorption, $v^{(-)}$ and $v^{(+)}$, the rest-frame equivalent widths, W_r, and the optical depth mean system absorption redshifts, z_{abs}, using the Lyα absorption feature.

For an absorption feature to be adopted as a detection, we apply the criterion of a 3 σ equivalent width significance level, i.e., $W_r \geq 3\sigma_{W_r}$, otherwise we quote $3\sigma_{W_r}$ as the upper limit on W_r. The quoted uncertainties in the measured equivalent widths account for both the pixel statistical uncertainty and the systematic uncertainty due to the choice of continuum fit. The latter assumes a mean continuum placement uncertainty of 30% of the mean pixel statistical uncertainty (see Sembach & Savage 1992). Depending on the signal-to-noise ratio of the spectral region, the continuum uncertainty yields a 5–20 mÅ systematic uncertainty in the equivalent width.

To verify the identity of Lyα absorption, we examine whether the associated Lyβ absorption is formally detected. Further verification is obtained by detection of the O VI doublet; however, not all Lyα absorption has detected Lyβ and/or metal-line absorption. In the case of the O VI doublet, we do not require that both members of the doublet are formally detected in order to identify either O VI λ1031 or O VI λ1037

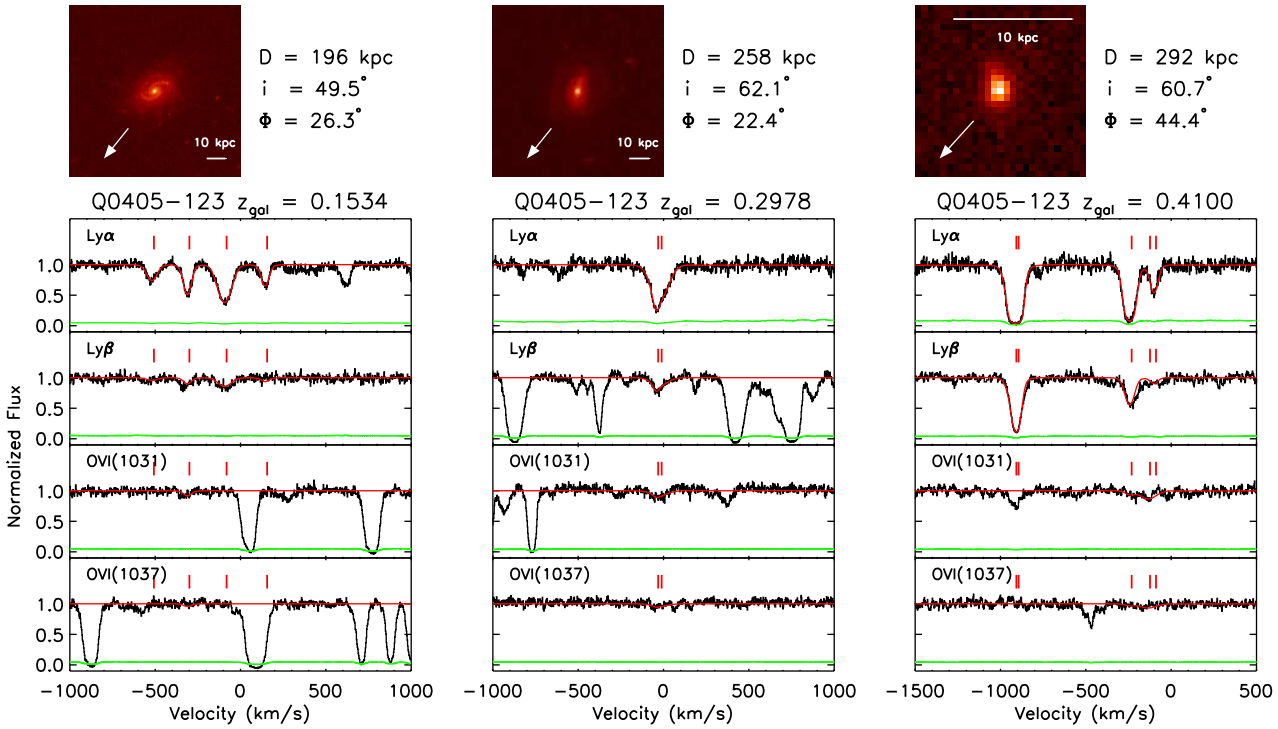

Figure 1. Galaxy and absorption data for the galaxies at z_{gal} = 0.1534, z_{gal} = 0.2978, and z_{gal} = 0.4100 in the field toward Q0405–123. We show the *HST*/WFPC2 image with an arrow pointing in the direction of the quasar sightline. The galaxy impact parameter, inclination, and azimuthal angle are listed. We also show the observed spectra and Voigt profile fits for the associated absorption. Plotted in black is the normalized, continuum-fitted UV spectrum and in green is the 1 σ uncertainty spectrum. Overlaid in red is the VP model fit for each transition. Red ticks mark the centroid of each VP component. Velocities are rest-frame relative to the associated galaxy systemic velocity.

absorption (either due to line blending or the λ1037 absorption being below the required significance level). The Lyα transition was detected for all but one of the galaxy-absorber pairs. For all but four galaxy-absorber pairs, Lyβ was detected, but O VI was detected for three of these four pairs. For only one pair, no Lyα, Lyβ, nor O VI was detected.

To quantify the absorption column densities and kinematics, we fitted the absorption line using Voigt profile (VP) decomposition. Each VP component is described by three physical parameters, the column density, Doppler *b* parameter, and the velocity center. We employed the code MINFIT (Churchill & Vogt 2001), adopting the philosophy of enforcing the minimum number of statistically required VP components to model an absorption system (i.e., simultaneously to all transitions). Details of the fitting procedure are described in Evans (2011). We tie the velocity centers for each VP component across all ions. We also assume the line broadening is dominated by a Gaussian turbulent component; therefore, each VP component at a given velocity has the same Doppler *b* parameter. The latter assumption is motivated by the simulations of Oppenheimer & Davé (2009) in which sub-resolution turbulence was required for modeling O VI absorbing gas in order to reproduce the observed column density and *b* parameter distributions. The one exception is z_{gal} = 0.1963 absorption in the spectrum of Q1259+5920, where a satisfactory VP model required thermal scaling of the Doppler *b* parameters.

Though Lyγ is detected for several, but not all of the absorption systems, we quote VP model results only from simultaneous fits to the Lyα and Lyβ transitions (except in three systems in which only Lyα was detected). Muzahid (2014) showed that Lyα and Lyβ absorption primarily traces the high ionization phase where O VI arises, whereas the higher order Lyman series line profiles are dominated by the lower ionization phase giving rise to C II, Si II, C III, and Si III absorption. Thus, by omitting higher order Lyman series lines we do not lose information on the O VI phase. Most importantly, by omitting higher order H I Lyman series lines, even when they are detected, we present a uniform analysis of the absorption systems. In Appendix B, we compare the derived H I column densities, N(H I), obtained from Lyα+Lyβ VP models and Lyα+Lyβ+Lyγ VP models for systems for which Lyγ is also detected. The exercise demonstrates that the inclusion of Lyγ does not discernibly alter our derived N(H I) values.

In the case of line blending (overlapping absorption from transitions associated with systems at other redshifts), when possible, we carefully decompose the lines using the procedure illustrated in Appendix C. The deblending technique is designed to recover the shape of the profile for the target transition.

Results of the absorption line analysis are listed in Table 3. Column (1) gives the quasar field. Columns (2) and (3) list the spectroscopic galaxy redshift and the absorption redshift. Columns (4)–(6) list the measured rest-frame equivalent widths of the Lyα, Lyβ, and O VI λ1031 absorption profiles. Columns (7) and (8) give the system total H I and O VI column densities, which are the sums of the VP components in each system. Columns (9) and (10) list the maximum blueward and redward velocity limits of the Lyα absorption profiles.

The range of rest-frame equivalent widths is $0.05 \leq W_r(\mathrm{Ly}\alpha) \leq 1.54$ Å and $0.02 \leq W_r(1031) \leq 0.45$ Å, corresponding to the system total column densities ranges $13.1 \leq$

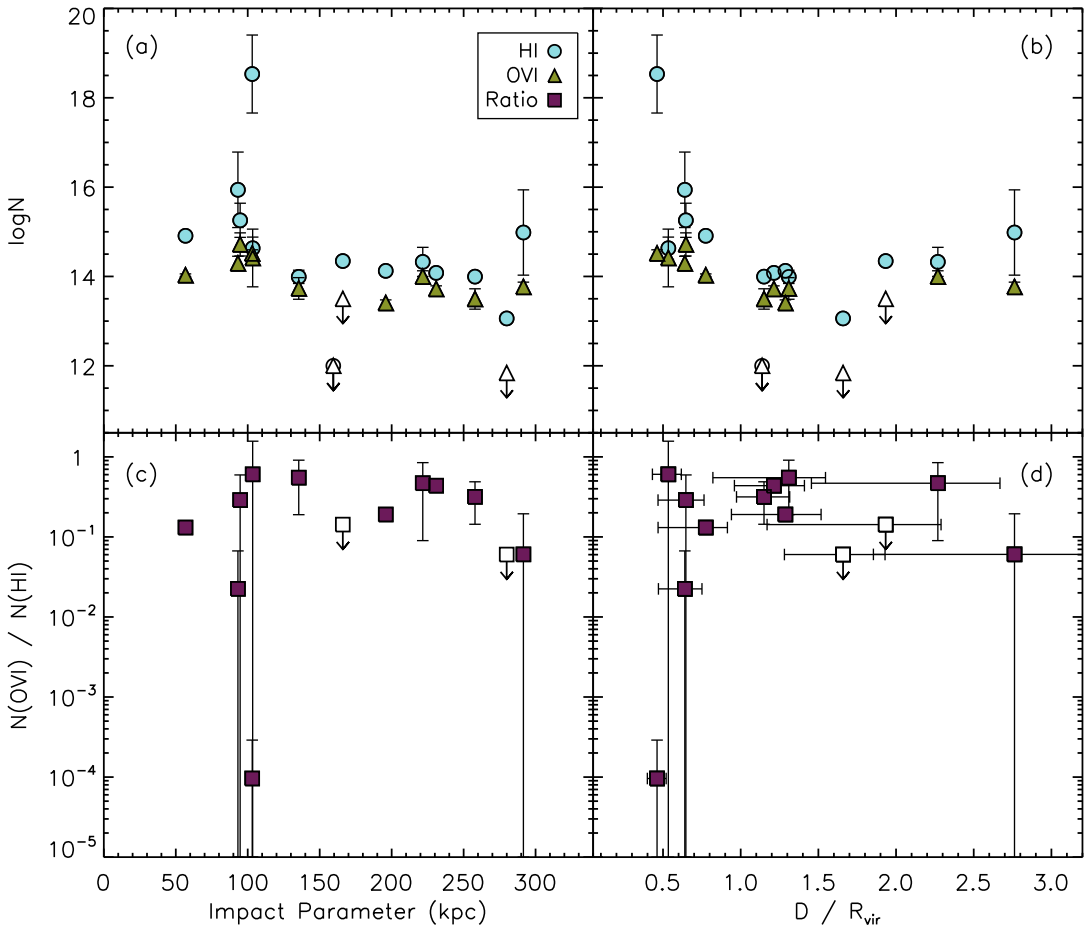

Figure 2. The system total N(H I) [sky-blue points], N(O VI) [green], and ratio N(O VI)/N(H I) [magenta] plotted against D [panels (a) and (c)] and against $D/R_{\rm vir}$ [panels (b) and (d)]. Open circles with downward arrows represent upper limits. The uncertainties in D are less than 1 kpc. The uncertainties in $D/R_{\rm vir}$ are shown in panel (f) only.

$\log N({\rm H\,I}) \leq 18.5$ and $13.4 \leq \log N({\rm O\,VI}) \leq 14.7$, respectively. The maximum blueward and redward velocities of the Lyα absorption are $v^{(-)} = -1020$ km s^{-1} and $v^{(+)} = 440$ km s^{-1}, respectively.

2.4. *Presentation of Galaxy-Absorber Pairs*

In Figure 1, we show three of the 14 galaxy-absorber pairs in our sample. The remaining 11 galaxies and their associated absorption are presented in Appendix A.

For each galaxy-absorber pair, we present a portion of the *HST*/WFPC2 image centered on the galaxy and the Lyα, Lyβ, and O VI $\lambda\lambda$1031, 1037 absorption profiles. In the galaxy image, the arrow points in the direction of the quasar line of sight. A bar provides that scale of 10 kpc in the galaxy rest frame. The legend provides the galaxy impact parameter, D, inclination, i, and azimuthal angle, Φ. The Voigt profile models of the absorption lines are the red curves superimposed on the black data. The velocity centroid of each VP component is shown by the red ticks above the continuum normalized spectra. The velocity zero-point of each spectrum is taken to be galaxy systemic velocity.

3. CGM EXTENT AND GEOMETRY

3.1. *Spatial Behavior*

In Figure 2, we present the spatial behavior of the system total H I column density, N(H I), and the system total O VI column density, N(O VI). The system total column densities are the sums of the individual Voigt profile component column densities. We color the N(H I) points sky-blue, the N(O VI) points green, and the ratio N(O VI)/N(H I) magenta. Upper limits are shown as open circles with downward arrows.

In Figure 2(a), we plot N(H I) and N(O VI) versus impact parameter, D. The total N(H I) is typically $\log N({\rm H\,I}) = 14$ out to $D \sim 300$ kpc (we note that one system has a stringent upper limit of $\log N({\rm H\,I}) < 12$). Though higher N(H I) systems are found at $D < 100$ kpc, there is no statistical trend between N(H I) and D. A Kendall-τ rank correlation test, which includes upper limits, yields a 1.8 σ consistency with the null hypothesis of no correlation.

We find N(O VI) out to $\sim$290 kpc to a limit of $\log N({\rm O\,VI}) = 12.8$. We note that the detection at D = 292 kpc (in Q0454–132 at z = 0.4100) is very tentative (see Figure 1). If that detection were deemed an upper limit, then our data show O VI absorption out to $\sim$260 kpc. Similar to the behavior with N(H I), we find no statistically significant trend between N(O VI) and D (only a 2.5 σ trend).

In Figure 2(b), we plot N(H I) and N(O VI) versus $D/R_{\rm vir}$. There is a higher average value and a broader spread in N(H I) for $D/R_{\rm vir} < 1$ as compared to $D/R_{\rm vir} > 1$, with $\log\langle N({\rm H\,I})\rangle =$

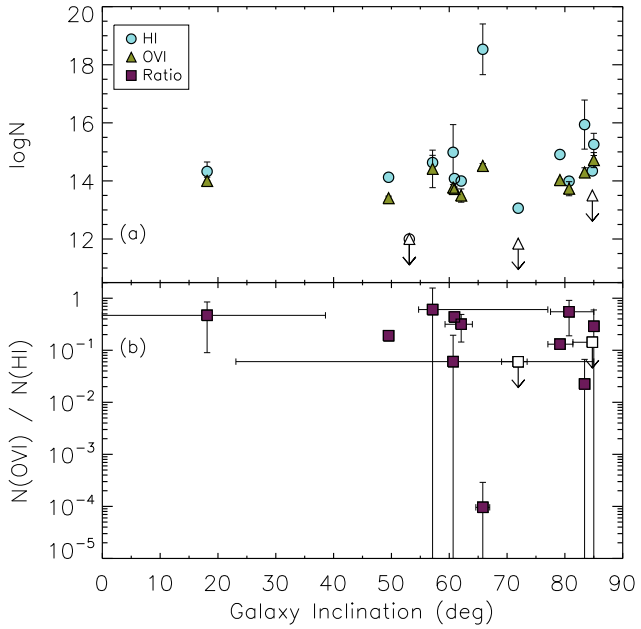

Figure 3. (a) The system total N(H I) [sky-blue] and N(O VI) [green] plotted against inclination i. (b) The ratio N(O VI)/N(H I) [magenta] plotted against inclination. Open circles with downward arrows represent upper limits. The uncertainties in the inclination are shown in panel (b) only.

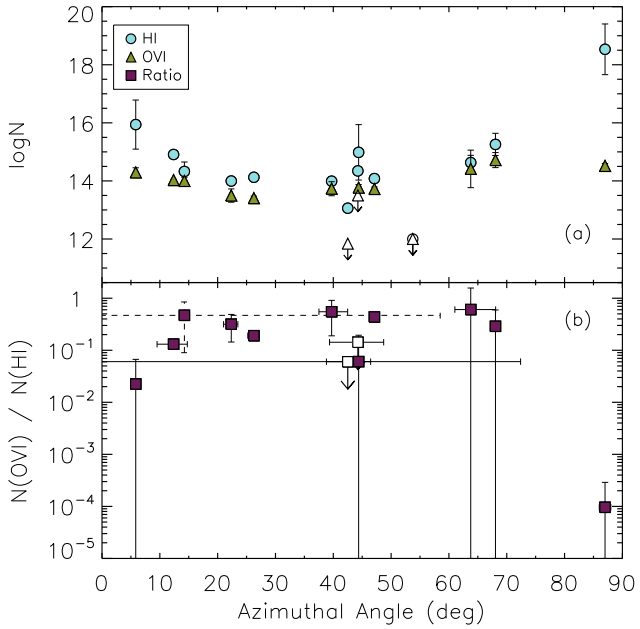

Figure 4. (a) The system total N(H I) [sky-blue] and N(O VI) [green] plotted against azimuthal angle, Φ. (b) The ratio N(O VI)/N(H I) [magenta] plotted against azimuthal angle. Open circles with downward arrows represent upper limits. The uncertainties in the azimuthal angle are shown in panel (b) only.

15.9 ± 1.6 inside the projected virial radius and $\log\langle N(\mathrm{H\,I})\rangle = 14.1 \pm 0.5$. outside the projected virial radius. In We find that the N(O VI) values inside and outside of the projected virial radius lie within one standard deviation of the average $\log\langle N(\mathrm{O\,VI})\rangle = 14.03 \pm 0.44$. We do not see a larger dispersion in N(O VI) at $D/R_{\rm vir} < 1$ as seen for H I.

The ratio N(O VI)/N(H I) is shown in Figures 2(c) and 2(d) as a function of D and $D/R_{\rm vir}$, respectively. Due to the flat spatial distribution of N(O VI) and the higher dispersion of N(H I) at $D/R_{\rm vir} < 1$, the spread in N(O VI)/N(H I) is a factor of $\simeq 8$ greater inside than outside the projected virial radius, with $\sigma(D/R_{\rm vir} \leq 1) = 1.5$ and $\sigma(D/R_{\rm vir} > 1) = 0.18$.

The different spreads in the N(O VI)/N(H I) inside and outside the projected virial radius are driven by the spatial behavior of H I. Inside the projected virial radius, N(H I) has a larger dispersion than outside this region, whereas N(O VI) has a small dispersion both inside and outside the projected virial radius. The O VI column densities inside the projected virial radius appear to be similar to those outside this region, whereas the quantity of H I can be variable.

3.2. *Galaxy Orientation*

To ensure we have a fair sample with which we can examine the geometric distribution of H I and O VI absorption around the galaxies, we performed Kolmogorov-Smirnov (KS) tests to determine whether the observed distributions of galaxy azimuthal angles, Φ, and inclinations, i, are consistent with being drawn from the distributions expected for an unbiased sample. For Φ, the KS test probability is P(KS) = 0.62 and for i the probability is P(KS) = 0.46. We conclude that both Φ and i are consistent with unbiased distributions.

In Figure 3(a) and 3(b), we show the system total N(H I), N(O VI), and N(O VI)/N(H I), respectively, versus inclination. The uncertainties in the inclination measurements derived from GIM2D are shown only in Figure 3(b). A Kendall-τ test (including limits) yields no trend in the N(H I) distribution ($1.1\,\sigma$), the N(O VI) distribution ($0.8\,\sigma$), nor in the distribution of the ratio N(O VI)/N(H I) ($0.8\,\sigma$) with galaxy inclination. Whether a galaxy is observed with a face-on or an edge-on orientation, there appears to be a relatively flat distribution of H I and O VI column densities.

In Figure 4(a) and 4(b), we present the system total N(H I), N(O VI), and N(O VI)/N(H I), respectively, versus azimuthal angle, Φ. The uncertainties in the azimuthal angle measurements derived from GIM2D are shown only in Figure 4(b) but apply for all panels. A Kendall-τ test (including limits) yields no statistical signature for a correlation between H I column density and Φ ($0.4\,\sigma$). We do note that the N(H I) values appear to increase toward the projected major axis ($\Phi = 0°$) and the projected minor axis ($\Phi = 90°$).

To crudely estimate the degree to which the two largest N(H I) absorbers (which are most closely aligned with the projected axes) may be outliers of the distribution of H I absorbers, we calculated the mean and standard deviation of the N(H I) excluding the two largest N(H I) absorbers. We obtained $\log\langle N(\mathrm{H\,I})\rangle = 14.47 \pm 0.74$. The two largest N(H I) absorbers lie at $2.8\,\sigma$ and $5.5\,\sigma$ from $\langle N(\mathrm{H\,I})\rangle$. For this small sample, the N(H I) of the system most closely aligned with the projected minor axis is an outlier of the N(H I) distribution in that it has a significantly larger column density. A statistical signature for an H I column density enhancement toward the projected major axis is less convincing.

We further examine the apparent trend for increasing N(H I) toward the projected major and minor axes by symmetrically folding the azimuthal angle about 45°, such that 0° corresponds to alignment along either the major or the minor projected axis and 45° corresponds to a 45° azimuthal angle with respect to either axis. A Kendall-τ test (including limits) on the folded distribution yields no statistical signature for an anti-correlation between N(H I) and angular separation away from the galaxy projected axes ($1.7\,\sigma$). If a trend exists, our sample is too small to reveal a statistical significance.

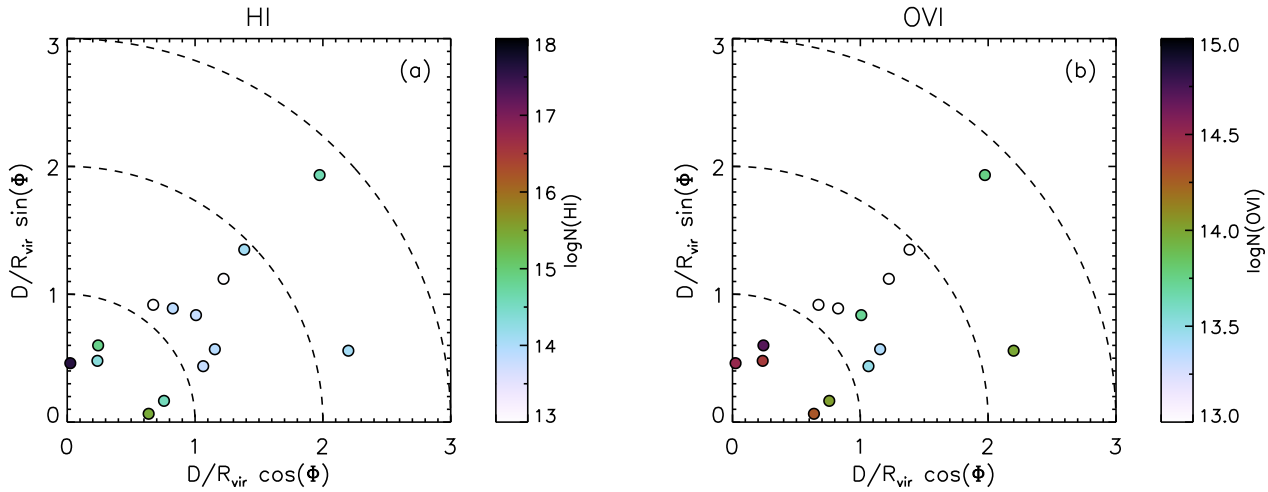

Figure 5. Projected azimuthal and $D/R_{\rm vir}$ cloud locations for (a) H I and (b) O VI. The horizontal axis represents the projected major axis and the vertical axis represents the projected minor axis. The dashed lines represent curves of constant $D/R_{\rm vir}$. Data points are colored according to the total system column density. Column density upper limits are plotted as open circles.

In the case of O VI, the azimuthal distribution of N(O VI) appears uniform, or flat, for all galaxy orientations. Computing the mean and standard deviation (omitting limits), we obtain $\log\langle N(\mathrm{O\,VI})\rangle = 14.05 \pm 0.42$ and find no outlying measurements with detected O VI absorption.

For the ratio N(O VI)/N(H I), the two absorbers within $\pm 10^\circ$ of the major and minor axes show a smaller ratio compared to the data in the range $10^\circ \leq \Phi \leq 80^\circ$. Excluding these two absorbers and the two absorbers with upper limits, the mean and standard deviation is $\log\langle N(\mathrm{O\,VI})/N(\mathrm{H\,I})\rangle = -0.61 \pm 0.45$. Compared to this distribution, the $\Phi \simeq 6^\circ$ absorber is a $\sim 4\,\sigma$ outlier and the $\Phi \simeq 87^\circ$ absorber is a $\sim 8\,\sigma$ outlier. Since the N(O VI) distribution is flat with azimuthal angle, whereas the N(H I) distribution exhibits higher values near the projected axes, the smaller N(O VI)/N(H I) ratios in these two absorbers are driven by their higher N(H I). We infer that the chemical and/or ionization conditions of the hot CGM are globally distributed, if patchy, for all azimuthal angles more than $\pm 10^\circ$ away from the projected major and minor axes (acknowledging some variation as suggested by the few upper limits).

3.3. *Distance and Orientation*

For visualization purposes, in Figure 5(a) and Figure 5(b), we illustrate the relationship between the two-dimensional projected location of the absorbing gas and the system total N(H I) and N(O VI), respectively. The projected geometric position of the quasar sightlines are computed with respect to the virial radius using the relations $D/R_{\rm vir}\cos(\Phi)$ for projection along the galaxy major axis, and $D/R_{\rm vir}\sin(\Phi)$ for projection along the galaxy minor axis. Data point colors correspond to absorber column density according to the color scale on the right. Upper limits are plotted as open circles.

Most galaxies probed at $D/R_{\rm vir} > 1$ in this sample have moderate column density absorption with $\log N(\mathrm{H\,I}) \simeq 14$ located at intermediate azimuthal angles, between 10° and 90°. In turn, the galaxies probed at $D/R_{\rm vir} < 1$ exhibit high column density absorption along their projected major and minor axes. Though the sample is small and the realization of the data may not be a full representation of a larger sample, our data suggest a picture in which moderate column density H I and O VI gas is distributed around galaxies out to greater than $2R_{\rm vir}$, with higher column density H I aligned near the galaxy projected major and minor axes for $D < R_{\rm vir}$.

4. KINEMATICS AND VIRIAL MASS

Characterizing the velocity distribution of the hot CGM is instrumental for determining the physical origin and fate of both H I and O VI absorbing gas in galactic environments. If the material is outflowing, velocity flows less than the galaxy halo escape velocity might trace gas that is likely to recycle back into the ISM and fuel star formation, whereas velocity flows greater than the escape velocity might leave the CGM permanently and chemically enrich the IGM. If the material is infalling from the IGM (or from satellite merging), the velocity distribution would provide insights into mechanisms of how such gas mixes with the hot CGM or eventually accretes into the ISM.

4.1. *Completeness*

The detection threshold sensitivity for absorption is not uniform from absorber to absorber due to varying signal-to-noise ratios, S/N, of the quasar spectra. Thus, for example, weak absorption at high relative velocity that could be detected in a high S/N spectral region for one system, might not be detectable for a different system appearing in a lower S/N spectral region. In conducting our kinematic analysis, we first examine the non-uniformity of the detection sensitivity.

In Figure 6, we present the cumulative distribution (CDF) of the 3 σ equivalent width detection limits for both Lyα and O VI λ1031 absorption. The detection thresholds are the 3 σ equivalent width uncertainties for unresolved lines (cf., Schneider et al. 1993; Churchill et al. 2000) averaged over ± 1000 km s^{-1} relative to the galaxy redshift assuming unresolved absorption lines. The sample is 100% complete for absorption features greater than $W_r(\mathrm{Ly}\alpha) = 0.062$ Å and $W_r(1031) = 0.032$ Å, indicating that we generally have higher S/N spectral coverage for O VI absorption. All but two of the individual absorption features in the sample have measured equivalent widths above the 100% completeness level. For our analysis, we removed these two features.

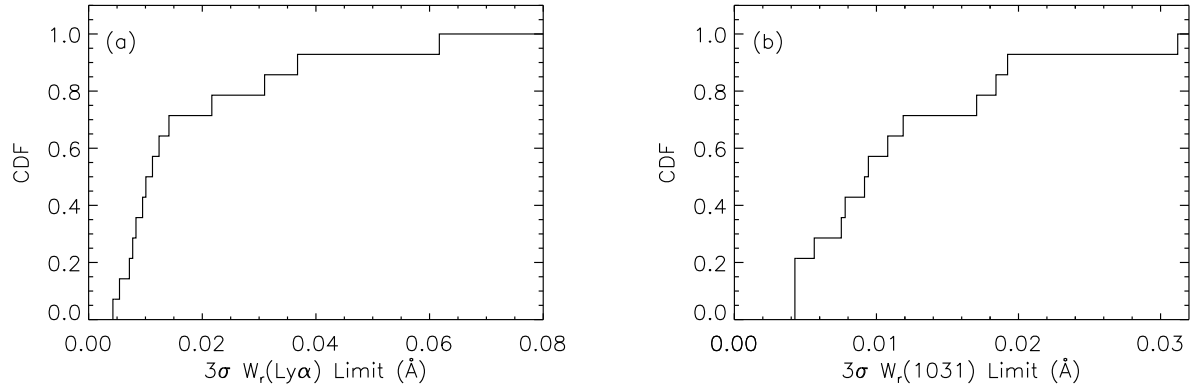

Figure 6. Cumulative distribution function of the equivalent width detection limit in (a) the Ly α absorption, and (b) the O VI λ1031 absorption. Our sample has 100% completeness in the detection sensitivity to W_r(Ly α) = 0.062 Å and W_r(1031) = 0.032 Å. Only one Ly α absorption feature and one O VI λ1031 absorption feature are measured with equivalent widths below the 100% completeness sensitivity. We have omitted those two features from our kinematic analysis.

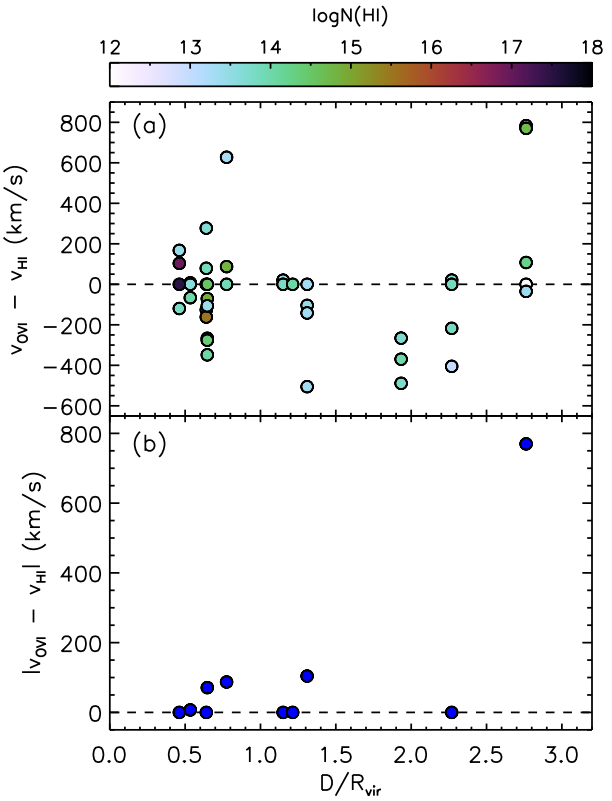

Figure 7. (a) The velocity offsets of the H I absorbing Voigt profile components "clouds" in a system with respect to the highest N(O VI) cloud in the system as a function of $D/R_{\rm vir}$. The colors of the data points are based upon the cloud N(H I) as given by the color bar legend. (b) The velocity offset between the highest N(O VI) cloud and the highest N(H I) cloud in a system as a function of $D/R_{\rm vir}$. In both panels, the dotted line at $v_{\rm OVI} - v_{\rm HI} = 0$ indicates no velocity offset.

4.2. *Kinematic Alignment of* H I *and* O VI

In Figure 7(a), we plot the velocity offset between the Voigt profile component "clouds" with the highest N(O VI) and each H I absorbing cloud as a function of $D/R_{\rm vir}$. The dotted line at $v_{\rm OVI} - v_{\rm HI} = 0$ indicates no velocity offset between the H I clouds and the highest N(O VI) cloud. Most H I and O VI absorbing clouds are clustered within $\sim$500 km s^{-1}.

The data also reveal that the highest N(O VI) cloud in a system does not align kinematically with the highest N(H I) cloud in every case. To further illustrate, we plot the velocity offset between the highest N(O VI) cloud and the highest N(H I) cloud in a system in Figure 7(b). In 5 of 10 systems with detected O VI absorption, we observe a velocity offset between the bulk of the neutral hydrogen and the bulk of the O VI. In three of these cases, the velocity offset is $\sim$100 km s^{-1}. Since a velocity offset implies spatially separated absorbing clouds, we can infer physically distinct phases of gas (different densities, temperatures, and metallicities) in roughly half of the sightlines through the CGM, as probed using O VI and H I as a tracer of the gas phase. Examining absorption from the low ions such as C II, Si II, etc., would be instrumental in examining whether this is the case. Unfortunately, the mean N(H I) for our sample is roughly 1.5 dex below the threshold where low ion metals can be detected in spectra with moderate signal-to-noise ratios (Hellsten et al. 1997).

4.3. *Kinematics and Escape Velocity*

In Figure 8, we plot the velocity difference between the individual Voigt profile component "clouds" and the galaxy systemic velocity, $\Delta v = v_{\rm cld} - v_{\rm gal} = c(z_{\rm cld} - z_{\rm gal})/(1+z_{\rm gal})$, as a function of halo mass, $M_{\rm h}$. Data point colors denote the $D/R_{\rm vir}$ location of the absorption, where sky-blue corresponds to $D/R_{\rm vir} \leq 1$, green between $1 < D/R_{\rm vir} \leq 2$, and $D/R_{\rm vir} > 2$ is magenta. For our sample, we find that $\sim$70% of H I absorbing components lie within $\pm$200 km s^{-1} of the galaxy systemic velocity, $\sim$80% lie within $\pm$300 km s^{-1}, and $\sim$90% lie within $\pm$500 km s^{-1}. For O VI, we find $\sim$90%, $\sim$95%, and 100% lie within $\pm$200, $\pm$300, and $\pm$500 km s^{-1}, respectively.

To investigate whether clouds have relative line of sight velocities that exceed or do not exceed the escape velocity of the halo in which they reside, we computed the escape velocity for each galaxy (cf., Steidel et al. 2010),

$$v_{\rm esc}^2(R) = \frac{2GM_{\rm h}}{R} \frac{\ln[1+c(R/R_{\rm vir})]}{\ln(1+c) - c/(1+c)}, \qquad (1)$$

for each galaxy at $R = R_{\rm vir}$, $2R_{\rm vir}$, and $3R_{\rm vir}$, where R is galactocentric distance, and superimposed the results on Figure 8 as colored lines corresponding to the three values of R. A Navarro et al. (1997) (NFW) dark matter halo profile is assumed with mean concentration parameter, $c(M_{\rm h}, z_{\rm gal})$, computed from the relation of Bullock et al. (2001). The curves are not smooth with increasing virial mass due to the redshift dependence of the concentration parameter.

The galactocentric distances of the clouds are not known, only constrained to lie at $R \geq D$. Assuming cloud galactocen-

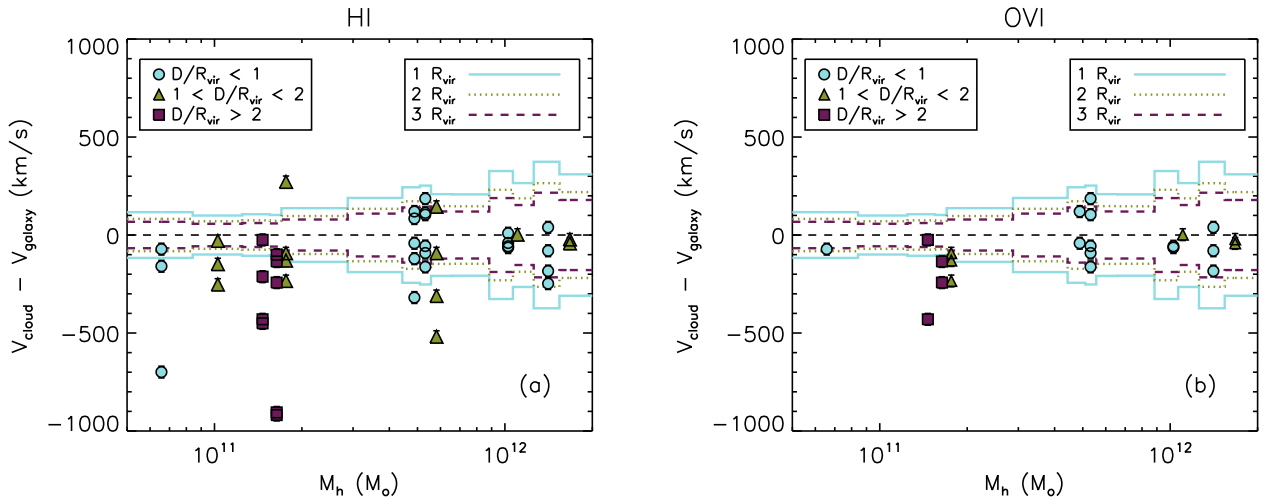

Figure 8. Individual Voigt profile component (cloud) velocity offsets with respect to the galaxy systemic velocity as a function of virial mass, $M_{\rm h}$. (a) H I clouds. (b) O VI clouds. Data are colored by $D/R_{\rm vir}$ bins. Vertical error bars are dominated by a $\simeq 30$ km s^{-1} uncertainty in the galaxy redshift. The colored lines are the escape velocities, $v_{\rm esc}$, for each galaxy computed using Equation 1 for assumed cloud galactocentric distances $R = R_{\rm vir}$, $2R_{\rm vir}$, and $3R_{\rm vir}$. At a given halo mass, points of a given color are to be compared to $v_{\rm esc}$ values having the same colored line.

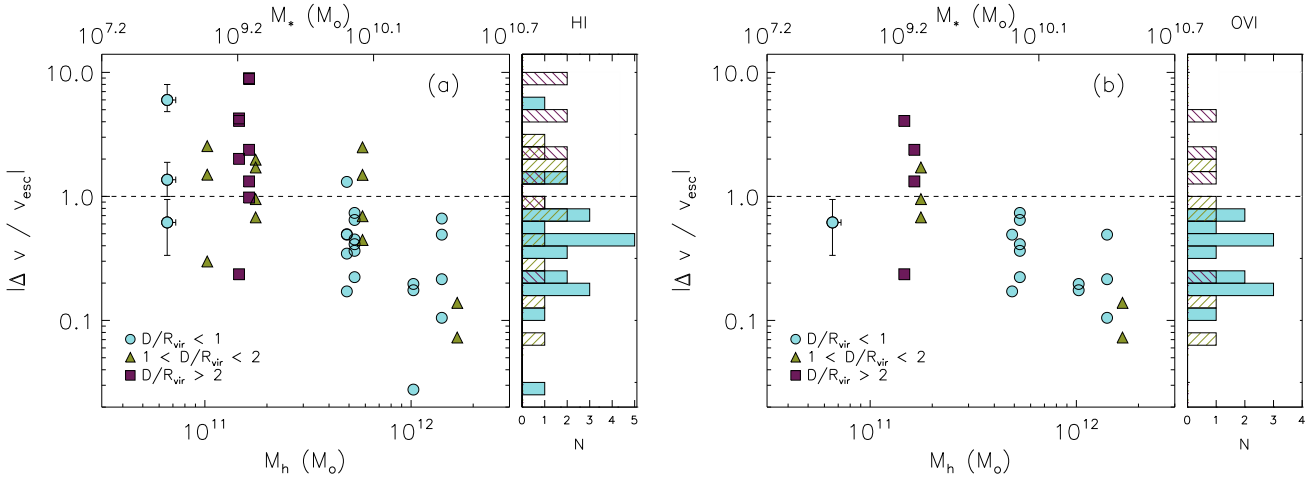

Figure 9. The absolute relative velocity of the Voigt profile "cloud" velocities with respect to the galaxy normalized to the escape velocity, $|\Delta v/v_{\rm esc}|$, as a function of virial and stellar mass, $M_{\rm h}$ and M_*. (a) H I clouds. (b) O VI clouds. Data are colored by $D/R_{\rm vir}$ bins using the same convention as for Figure 8. The escape velocity is computed assuming the clouds reside at galactocentric distance $R = D$, which yields lower limits on $|\Delta v/v_{\rm esc}|$. Representative error bars for $|\Delta v/v_{\rm esc}|$ are provided for the lowest virial mass galaxy and account for the $\simeq 30$ km s^{-1} uncertainty in the galaxy redshift and in the virial mass propagated through Equation 1. The horizontal dashed line at $|\Delta v/v_{\rm esc}| = 1$ represents cloud offset velocities equal to the halo escape velocity. Histograms (right subpanels) provide the number of clouds in equal logarithmic bins for all virial masses. The fraction of clouds with velocity offsets greater than the halo escape velocity increases with decreasing stellar and halo mass.

tric distances at multiples of the virial radius, and comparing same-colored points and curves, we find $\sim$40% of H I cloud components have relative velocities in excess of the galaxy escape velocity. Roughly 60% of the clouds that reside outside the virial radius (green and magenta data) have velocities exceeding the escape velocity, whereas only $\sim$15% of clouds, if they reside at the virial radius (sky-blue data/lines), have greater than escape velocities.

4.4. *Differential Kinematics*

In Figure 9, we show the absolute relative velocity of the absorption with respect to the galaxy normalized to the escape velocity, $|\Delta v/v_{\rm esc}|$, versus virial mass. We also show the galaxy stellar mass, M_*, based upon the stellar mass to halo mass functions of Moster et al. (2010). Data points are colored by $D/R_{\rm vir}$ using the same designations as in Figure 8. For this exercise, we assume $R = D$ for the absorbing clouds, which provides the upper limit to the escape velocity. Thus, the points plotted in Figure 9 are lower limits on $|\Delta v/v_{\rm esc}|$. Characteristic error bars are shown on the left-most data points in each panel. Points that lie above the dotted line at $|\Delta v/v_{\rm esc}| = 1$ are clouds that have velocities in excess of the galaxy escape velocity and, if outflowing, could be unbound. The histogram on the right shows the total number of clouds in $|\Delta v/v_{\rm esc}|$ bins for all halo masses.

For H I absorption, we computed the fraction of clouds with $|\Delta v/v_{\rm esc}| \leq 1$, i.e., those that can be inferred to be gravitationally bound to their host halo. We divide the sample of clouds into several subsamples based upon $D/R_{\rm vir}$ and virial mass, $M_{\rm h}$. The $D/R_{\rm vir}$ ranges are $(0,1]$, $(1,2]$, $(2,3]$, and $[0.3)$ for each mass range, $M_{\rm h} < 10^{11.5}$ M$_\odot$, $M_{\rm h} > 10^{11.5}$ M$_\odot$, and "all" $M_{\rm h}$, where $M_{\rm h} = 10^{11.5}$ M$_\odot$ is the median virial mass of the sample. Comparing the "bound fraction" in each of these subsamples allows a differential characterization of H I kinematics.

Table 4
Bound Fractions of H I Clouds

(1) $D/R_{\rm vir}$ range	(2) all $M_{\rm h}$ [$M_\odot$]	(3) $M_{\rm h} > 10^{11.5}$ [$M_\odot$]	(4) $M_{\rm h} < 10^{11.5}$ [$M_\odot$]
$0 < D/R_{\rm vir} \leq 1$	$0.85^{+0.08}_{-0.13}$	$0.94^{+0.05}_{-0.12}$	$0.33^{+0.41}_{-0.28}$
$1 < D/R_{\rm vir} \leq 2$	$0.54^{+0.17}_{-0.17}$	$0.67^{+0.21}_{-0.28}$	$0.43^{+0.25}_{-0.22}$
$2 < D/R_{\rm vir} \leq 3$	$0.11^{+0.21}_{-0.09}$	···	$0.11^{+0.21}_{-0.09}$
$0 < D/R_{\rm vir} \leq 3$	$0.59^{+0.09}_{-0.09}$	$0.87^{+0.07}_{-0.11}$	$0.26^{+0.14}_{-0.11}$

The H I cloud bound fractions are presented in Table 4. Column (1) lists the $D/R_{\rm vir}$ range, and columns (2), (3), and (4) list the bound fractions for the three mass ranges. The bound fractions are $n_1/(n_1+n_2)$, where n_1 is the number of clouds with $|\Delta v/v_{\rm esc}| \leq 1$ and n_2 is the number of clouds with $|\Delta v/v_{\rm esc}| > 1$. The quoted uncertainties assume a binomial distribution (see Gehrels 1986) and were computed using incomplete β functions for a confidence level of 84.13% (single sided 1 σ). We remind the reader that we measure line of sight velocities. Despite having constraints on the galaxy inclinations and azimuthal angles on the sky, deprojecting the gas velocities is an intractable problem due to significant uncertainty in the true gas motions which are a result of the complex interplay between outflow geometry, environmental conditions, and inflow dynamics.

Examining column (2) of Table 4, we find that the bound fraction decreases as $D/R_{\rm vir}$ increases. In other words, the proportion of clouds with greater than escape velocities increases with increasing projected distance relative to the virial radius. On average, $\sim$40% of the clouds could be inferred to be escaping the halo for $D/R_{\rm vir} \leq 3$ for all virial masses represented in the sample, assuming the clouds are outflows (we reserve further discussion on this point until Section 5.3).

Comparing columns (3) and (4) of Table 4, we find that, in each and every $D/R_{\rm vir}$ range, higher mass halos have a larger fraction of bound clouds than do lower mass halos. Or, alternatively, the fraction of clouds with $|v| > v_{\rm esc}$ is larger in lower mass halos than in higher mass halos. On average, $\sim$75% of the clouds have $|v| > v_{\rm esc}$ for lower mass halos, whereas only $\sim$10% of the clouds have $|v| > v_{\rm esc}$ for higher mass halos.

When interpreting the trends presented in Table 4, we must be careful to consider the selection effect that, in small samples characterized by a pre-selected D range, lower mass halos are preferentially probed at larger $D/R_{\rm vir}$ because they have smaller virial radii than larger mass halos. Thus, the majority of the absorbers in the $M_{\rm h} < 10^{11.5}$ $M_\odot$ subsample are probed at $D/R_{\rm vir} > 1$. The trend that the bound fraction decreases as $D/R_{\rm vir}$ increases may be enhanced in our sample due to the increase in the relative number of lower mass galaxies at larger $D/R_{\rm vir}$. This is corroborated by the result that higher mass halos have a larger fraction of bound clouds than do lower mass halos in each finite $D/R_{\rm vir}$ range, which likely does not suffer from any selection bias and is a more robust finding.

Examining O VI absorbers, we find associated O VI absorption in only $\sim$40% of the H I clouds in and around lower mass halos as compared to $\sim$85% around higher mass halos. Given the flat H I column density distribution for our sample, the lower number of detected O VI clouds in lower mass halos suggests conditions favoring higher O VI column densities are less common out to $D \simeq 300$ kpc of lower mass halos than for higher mass halos.

For O VI absorbers, as shown in Figure 9(b), the clouds have a bound fraction of $0.82^{+0.09}_{-0.12}$ for all halo masses in the sample. For higher mass halos, the bound fraction is $1.00^{+0.00}_{-0.12}$ and for lower mass halos the bound fraction is $0.50^{+0.22}_{-0.22}$. We thus can infer that O VI absorbing gas is more common in higher mass halos and is primarily bound to the halo, whereas O VI absorbing gas is less commonly found in the vicinity of lower mass halos and only half of the O VI absorbing clouds are bound.

5. DISCUSSION

5.1. *Spatial Extent of the Hot CGM*

Our small sample of 14 galaxy-absorber pairs is similar to that of the COS-Halos project (Tumlinson et al. 2013), but with a few differences. First, our sample probes H I and O VI absorption out to 300 kpc, whereas the COS-Halos sample probes out to 150 kpc. Second, our sample covers a slightly smaller range of virial mass, $10.8 \leq \log(M_{\rm h}/M_\odot) \leq 12.2$, as compared to COS-Halos, $11.3 \leq \log(M_{\rm h}/M_\odot) \leq 13.3$. We thus probe to 0.5 dex lower in virial mass, but do not probe the highest full decade of the COS-Halos sample. The redshift coverage is roughly identical to that of COS-Halos ($z \lesssim 0.3$), but for the single galaxy in our sample at $z = 0.66$.

We note that the selection criteria between the two surveys are not too dissimilar, since we also selected our galaxies with no *a priori* pre-disposition to H I absorption in the background quasar spectra. We do not have the data to estimate the specific star formation rates of the galaxies in our sample. However, since Tumlinson et al. (2013) conclude there is very weak evidence for a difference in the detection frequency of H I between "star-forming" and "passive" galaxies, there should be little-to-no ambiguity in comparing the neutral hydrogen between samples.

To a 3 σ equivalent width detection sensitivity of $W_r(\mathrm{Ly}\,\alpha) = 0.05$ Å (100% completeness, corresponding to $\log N(\mathrm{H\,I}) = 13$ for $b = 30$ km s^{-1}), we find H I absorption is present out to 300 kpc for 13 of 14 galaxies in our sample, indicating that H I gas is clearly present out to $\sim$3 projected virial radii. For $D/R_{\rm vir} < 1$, we measure a mean system total column density of $\log\langle N(\mathrm{H\,I})\rangle = 15.9 \pm 1.6$, which is in good agreement with the column densities found in this region for the COS-Halos sample, which probes out to $D/R_{\rm vir} \simeq 0.75$. For $D/R_{\rm vir} > 1$, we find $\log\langle N(\mathrm{H\,I})\rangle = 14.1 \pm 0.5$, a value $\simeq 1.8$ dex lower. This behavior would suggest a transition at $D/R_{\rm vir} \simeq 1$ in the physical nature of H I, possibly due to a changes in cloud densities, sizes, or ionization conditions.

The behavior of H I that we described above is consistent with the conclusion drawn from Tumlinson et al. (2013), that there is significant "evolution" in the H I properties between the regions $D < 200$ kpc and outside this region, as based upon their comparison with several other studies of H I absorption around galaxies (see their Section 5.1). In our smaller sample representing the lower mass range of COS-Halos, this "evolution", or transition, appears to set in at $D \simeq 100$ kpc. This could imply that lower mass halos have smaller physical extent than higher mass halos (also see Churchill et al. 2013b; Ford et al. 2013). Consistent with the conclusions of Tumlinson et al. (2013) and Stocke et al. (2013), we also infer that, based upon the behavior of H I absorption, the virial radius appears to be a transition region between the CGM and the IGM. Our data suggest this region is quite extended and is not abrupt. However, this does not preclude that possibility that metals from the ISM are being transported through the CGM to several virial radii and out to the IGM.

To a 3 σ detection sensitivity of $W_r(1031) = 0.032$ Å (100% completeness, corresponding to $\log N(\mathrm{O\,VI}) = 13.5$ for b = 20 km s^{-1}), we find O VI absorption is present out to the impact parameter limit of our survey ($\sim$300 kpc) for 11 of 14 galaxies in our sample. This corresponds to O VI absorption as far out as $D/R_{\rm vir} \simeq 2.7$, which could suggest that O VI enrichment for the host galaxy as far as $\sim$3 virial radii. We do not find an anti-correlation for N(O VI) with D nor with $D/R_{\rm vir}$, though the five detections at $D/R_{\rm vir} < 1$ are the five highest N(O VI) absorbers.

Out to their survey limit of D = 150 kpc ($D/R_{\rm vir} \simeq 0.75$), COS-Halos finds that O VI absorption with $\log N(\mathrm{O\,VI}) \geq 14.2$ is preferentially found in the CGM of star forming galaxies (Tumlinson et al. 2011). As stated above, we cannot address a comparison between O VI absorption and the star forming properties of the galaxies in our smaller sample. However, it would be interesting to do so given our deeper detection sensitivity to O VI absorption. COS-Halos is roughly 20% complete (9/42) for detections below $\log N(\mathrm{O\,VI}) = 14.0$ and 100% complete to $\log N(\mathrm{O\,VI}) = 14.2$, whereas we are 100% complete to $\log N(\mathrm{O\,VI}) = 13.5$. Of interest is that the "passive" galaxies are among the most massive galaxies in the COS-Halos sample and lie in the mass range not represented in our sample. If we speculate that this implies our lower mass galaxies are drawn from the same population as the star-forming population represented in the COS-Halos survey, then we have found examples where the CGM of star forming galaxies can have detectable absorption weaker than $\log N(\mathrm{O\,VI}) = 14.2$.

We find that the distribution of the total system ratio $N(\mathrm{O\,VI})/N(\mathrm{H\,I})$ is consistent with being flat out to D = 290 kpc and $D/R_{\rm vir} \simeq 2.7$. However, in terms of individual clouds (VP components), there is a higher incidence of O VI absorption in H I clouds for higher mass halos than in lower mass halos. Dividing the sample by the median virial mass of $\log M_{\rm h}/M_{\odot} = 11.5$, O VI absorption is found in only $\sim$40% of the H I clouds in the around lower mass halos as compared to $\sim$85% around higher mass halos. Since the system total N(H I) is fairly flat, the smaller fraction of detected O VI clouds in lower mass halos suggest conditions favoring O VI are less common out to $D \simeq 300$ kpc of lower mass halos than for higher mass halos.

5.2. *Geometric Distribution of the Hot CGM*

Using Mg II absorbers, Kacprzak et al. (2012a) and Bouché et al. (2012) have shown cool/warm CGM gas is more frequently found to be aligned with either the galaxy projected major or minor axes. Bordoloi et al. (2011) finds stronger Mg II is preferentially aligned with the projected minor axis. Kacprzak et al. (2011) find that Mg II equivalent widths correlate with galaxy inclination when scaled by the impact parameter. Based upon these results, the authors have suggested wind driven material may be responsible for the enhanced absorption strengths aligned with the galaxy minor axes, whereas the inclination correlation may indicate a planer distribution (also seen as a projected major axis alignment) of absorbing gas, perhaps accreting from the IGM.

For our sample, our data suggest that higher H I column density gas is preferentially found within $\pm 10^{\circ}$ of the major and minor axes (inside the projected virial radius). However, this is not a statistically significant result.

In the case of O VI, as seen in Figure 4(b), the azimuthal distribution of N(O VI) is statistically consistent with being flat. However, the ratio $N(\mathrm{O\,VI})/N(\mathrm{H\,I})$ for the two absorbers within $\pm 10^{\circ}$ of the major and minor axes have the smallest values and are statistical outliers (to better than 4 σ) as compared to the values in the range $10^{\circ} \leq \Phi \leq 80^{\circ}$. This would suggest that, on average, the chemical and/or ionization conditions of the hot CGM are fairly uniform in their geometrical distribution around galaxies for azimuthal angles more than $\pm 10^{\circ}$ away from the projected major and minor axes (acknowledging some variation as suggested by the fact that not all H I clouds exhibit O VI absorption).

The higher H I column density gas clouds with lower $N(\mathrm{O\,VI})/N(\mathrm{H\,I})$ ratios, but with typical N(O VI), that reside within $\pm 10^{\circ}$ of the major and minor axes, may reflect the presence of multi-phase gas at these geometric projections, with most of the H I associated with higher density, lower ionization gas. The ionization conditions, densities, and temperatures of the $\Phi \simeq 87^{\circ}$ (minor axis aligned) absorber (Q1317+2743 at z = 0.6605) are clearly multi-phase in nature (Kacprzak et al. 2012b). No detailed study has been conducted on the $\Phi \simeq 6^{\circ}$ (major axis aligned) absorber (Q1136–1334 at z = 0.2044). However, the COS/G130M spectrum covers several low and intermediate ionic transitions, including but not limited to C II λ1035, C III λ977, Si II $\lambda\lambda$1190, 1193, and Si III λ1206. Of these, C III and Si III are clearly detected in absorption, C II may be weakly detected, and Si II resides in a very noisy region of the spectrum.

We might infer that the two absorbers within $\pm 10^{\circ}$ of the major and minor axes have larger N(H I) columns because they are multi-phase systems, whereas the systems at greater angular separation from the galaxy projected axes trace the hot CGM. This would be consistent with the findings of Kacprzak et al. (2012a), who report an increase in the frequency of Mg II absorbers with azimuthal locations aligned with the projected major and minor axes. Unfortunately, the N(H I) values for the remaining absorbers in our sample are roughly 1.5 dex below the threshold where low ion metals can be detected, even for solar metallicity gas (Hellsten et al. 1997).

5.3. *Interpreting the Kinematics*

Constraining the galactocentric distances of the absorbing clouds is central to interpreting the differential behavior in the bound fraction of H I clouds (see Figure 9 and Table 4). The data place only lower limits of $R \geq D$ on their galactocentric distance and $R/R_{\rm vir} \geq D/R_{\rm vir}$ on their distances relative to the virial radius; we cannot definitively determine whether a given absorber arises in the IGM beyond $R = 4R_{\rm vir}$, where Hubble flow begins to dominate the peculiar velocities (see Cuesta et al. 2008).

Based upon SPH simulations, Oppenheimer & Davé (2009) argue that weaker O VI absorbers, $\log N(\mathrm{O\,VI}) \simeq 14$, may trace the old high-metallicity regions of the IGM and that many of these absorbers are not dynamically associated with the galaxy closest in projection on the sky. They find that many of the absorbers could have originated from a different galaxy at an earlier epoch and show (see their Figure 15) that weak O VI absorbers could arise between $1 \leq R/R_{\rm vir} \leq 10$, where R is the galactocentric distance. This range corresponds to 100 kpc $\leq R \leq$ 1 Mpc, depending upon the galaxy mass.

If we assume that clouds are not dynamically associated with their identified host galaxy and that the absolute velocity offset between a cloud and the "host" galaxy, $|\Delta v|$, is due to Hubble flow (with zero peculiar velocity), we can estimate R.

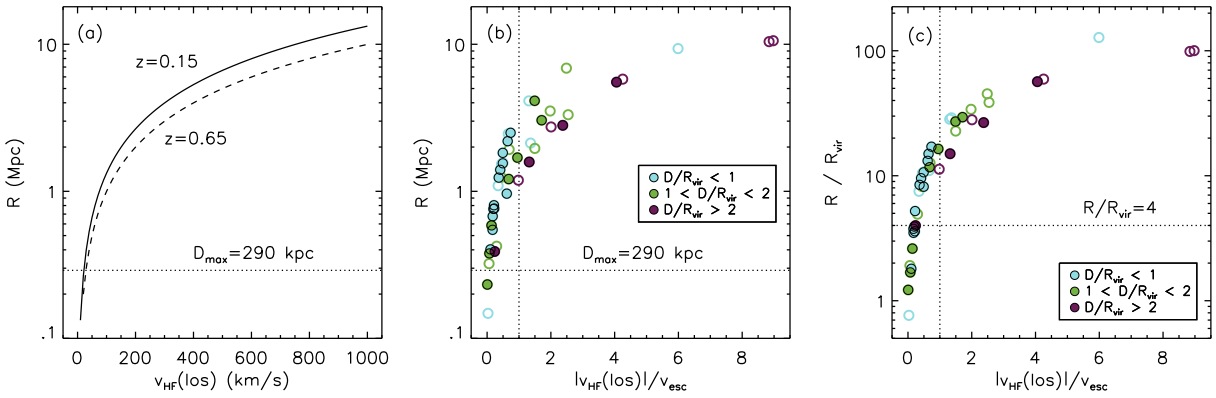

Figure 10. The proper galactocentric distances, R, to the absorbing clouds assuming that the observed cloud-galaxy velocity offsets are pure line of sight Hubble flow, i.e., $|\Delta v| = |v_{\rm HF}({\rm los})|$. (a) R versus $v_{\rm HF}({\rm los})$ for $z_{\rm gal} = 0.15$ and $z_{\rm gal} = 0.65$, illustrating Eq. 2. At each $z_{\rm gal}$, the curves are independent of D for $R \gg D$. The horizontal line at $R = D_{\rm max} = 290$ kpc indicates the maximum impact parameter of the sample. (b) R as a function of $|v_{\rm HF}({\rm los})|/v_{\rm esc}$ for the individual clouds in our sample. Points are colored by their $D/R_{\rm vir}$ location using the color scheme employed for Figures 8 and 9. Filled points are clouds for which O VI absorption is detected with the H I absorption and open points are H I only clouds. The vertical line is $|v_{\rm HF}({\rm los})|/v_{\rm esc} = 1$. (c) $R/R_{\rm vir}$ as a function of $|v_{\rm HF}({\rm los})|/v_{\rm esc}$. The vertical line is $|v_{\rm HF}({\rm los})|/v_{\rm esc} = 1$ and the horizontal line is $R/R_{\rm vir} = 4$, the spatial location around a halo where Hubble flow dominates over dark matter accretion.

The observer line of sight Hubble flow velocity[8] for a cloud with impact parameter D at galactocentric distance R from a galaxy at $z_{\rm gal}$ is

$$v_{\rm HF}({\rm los}) = H_0 E(z_{\rm gal}) R \sqrt{1-(D/R)^2}\,, \qquad (2)$$

where $E(z) = \sqrt{\Omega_m(1+z)+\Omega_\Lambda}$. In Figure 10(a), we plot R as a function of $v_{\rm HF}({\rm los})$ for $z_{\rm gal} = 0.15$ and $z_{\rm gal} = 0.65$, which bracket the redshifts of our sample. When $D/R \ll 1$, the curves are independent of D.

In Figure 10(b), we plot R as a function of $|v_{\rm HF}({\rm los})|/v_{\rm esc}$ for the individual clouds in our sample by assuming that the observed velocity offset of the cloud is pure line of sight Hubble flow, i.e., $|\Delta v| = |v_{\rm HF}({\rm los})|$. Points are colored by their $D/R_{\rm vir}$ location using the color scheme employed for Figures 8 and 9. Filled points are clouds for which O VI absorption is detected with the H I absorption, and open points are H I only clouds.

If the H I and O VI absorbing clouds are interpreted in the context of the predictions of Oppenheimer & Davé (2009) [see their Figure 15], we would expect the clouds reside within $R \leq 1$ Mpc of the galaxies. Figure 10(b) shows that, if the velocity offsets are due to Hubble flow, then 31 of 45 ($\sim 70\%$) absorbing clouds would be predicted to reside between 1 Mpc and 11 Mpc, and 13 of 24 ($\sim 50\%$) clouds with O VI absorption would be predicted to reside between 1 Mpc and 6 Mpc. Our O VI absorbing clouds, which have $\log N({\rm O\,VI}) \simeq 14$, would not be analogues of the "dynamically unassociated" O VI absorbers of Oppenheimer & Davé (2009) if they reside at $R > 1$ Mpc from their nearest projected galaxies.

The same conclusions can be inferred from Figure 10(c), in which we plot $R/R_{\rm vir}$ as a function of $|v_{\rm HF}({\rm los})|/v_{\rm esc}$. Using AMR cosmological simulations, Cuesta et al. (2008) showed that the influence of the halo gravitational potential on dark matter particles extends no farther than $R \simeq 4R_{\rm vir}$ for halo masses ranging from $10 \leq \log M_{\rm h}/M_\odot \leq 14$; Hubble flow dominates for $R/R_{\rm vir} > 4$ regardless of halo mass. As seen in Figure 10(c), if the velocity offsets are due to Hubble flow, then $\sim 70\%$ of the clouds and $\sim 60\%$ of the clouds with O VI absorption reside at $R/R_{\rm vir} > 4$. The 16 clouds with $|v_{\rm HF}({\rm los})|/v_{\rm esc} > 1$ would reside between $15 \leq R/R_{\rm vir} \leq 130$, and the 5 of these with O VI absorption would reside between $15 \leq R/R_{\rm vir} \leq 60$.

Based upon the above exercise, we must either adopt the interpretation that (1) the velocity offsets of more than half of the absorbing clouds in our sample are explained by Hubble flow and that they are IGM absorbers at Mpc distances well beyond $R = 15R_{\rm vir}$ from their identified galaxies, or (2) the clouds are in fact associated with their host galaxies and that the velocity offsets are peculiar velocities due to physical and dynamical processes within $R \simeq 4R_{\rm vir}$. As we discuss below, our exercise leaves very little room for ambiguity between these very different scenarios.

The surveys of Tripp et al. (2001, 2006), and Tumlinson et al. (2005, 2011) have shown that the nearest projected neighboring galaxies are within 200 kpc of O VI absorbers. Stocke et al. (2006) finds that, for $\log N({\rm O\,VI}) \geq 13.2$, the median distance of O VI absorbers from the nearest projected galaxy is 350-500 kpc for L^* galaxies and 200-270 kpc for 0.1 L^* galaxies. In addition, we note that if O VI absorbers with column densities in the regime detected in our survey are in the IGM at Mpc distance from galaxies, then the covering fraction of O VI absorbers should have no dependence on galaxy property. However, precisely the opposite is observed in that Tumlinson et al. (2011) reports a reduced frequency of O VI absorbers in the vicinity of galaxies with lower specific star formation rates, at least for $\log N({\rm O\,VI}) \geq 14.2$ within $D = 150$ kpc. Finally, we argue that, if the transition from the CGM to the IGM occurs at an overdensity of $\log \rho_{\rm H}/\bar{\rho}_{\rm H} \simeq 0.5$, as indicated by the observations of Steidel et al. (2010), Prochaska et al. (2011), and Rudie et al. (2012) and cosmological simulations such as those of Davé et al. (1999), then the IGM at $z < 0.5$ would correspond with $\log N({\rm H\,I}) \lesssim 13$. The individual clouds we are studying have $\log N({\rm H\,I}) \sim 14$ corresponding to $\log \rho_{\rm H}/\bar{\rho}_{\rm H} \simeq 1.3$, suggesting that they reside in the regime of $R/R_{\rm vir} \lesssim 4$ (Klypin et al. 2011). We conclude that it is unlikely that the absorbers in our sample reside at Mpc distances in the IGM or that their velocity offsets are due to Hubble flow.

Assuming the absorbing clouds are under the influence of

[8] The radial Hubble flow velocity of a source at z_s for an observer at z_o is $v_{\rm HF} = cE(z_o)D_c(z_o,z_s)/(1+z_o)$, where $D_c(z_o,z_s)$ is their radial comoving separation.

the halos of their host galaxies, we still cannot directly distinguish whether the clouds are outflowing or inflowing from the data themselves. However, simple gravitational energy conserving physical arguments can be invoked to show that infalling material is not expected to have velocity offsets with respect to the galaxy that exceed the halo escape velocity. First, material does not fall into halos from infinity, but from the "Eulerian sphere", a region with a $\sim$2 Mpc comoving radius that is set by the infall times being shorter than the Hubble time. Dark matter only ΛCDM cosmological simulations support such expectations (e.g., Cuesta et al. 2008). Though the infall velocities of a non-negligible fraction of the infalling dark matter particles exceed the circular velocity at the virial radius, virtually none exceed the escape velocity. Second, gas experiences hydrodynamic forces that act to decelerate infalling gas.

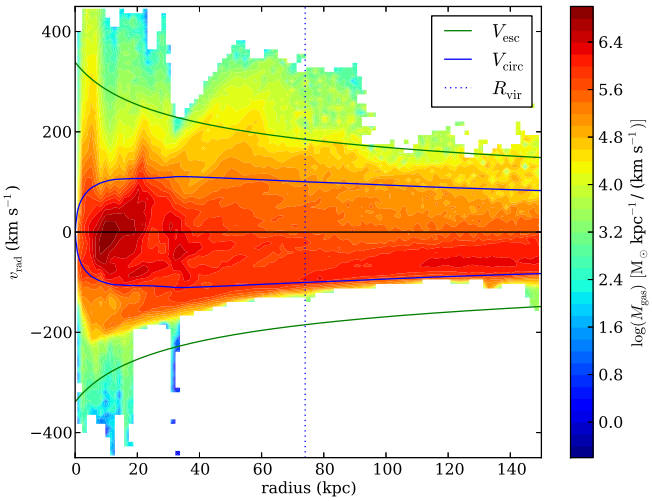

Figure 11. Radial velocity versus galactocentric radius of gas mass in units of solar masses per unit kpc per unit velocity (see the color bar) showing the outflow (positive velocities) and inflow (negative velocities) into a simulated galaxy with $M_{\rm h} \simeq 2 \times 10^{11}$ M$_\odot$. The vertical dotted line is the virial radius. The solid green curves represent the escape velocity as computed from Equation 1 and the blue curves represent the circular velocity. Note that the velocity of infalling gas does not exceed the escape velocity.

The kinematic behavior of gas can be examined in hydrodynamic + N-body ΛCDM cosmological simulations that compare various stellar feedback recipes (Trujillo-Gomez et al. 2014). We examined the gas kinematics in a simulated galaxy from the work of Trujillo-Gomez et al. (2013). We use the model spRP_40, which has virial mass $\log M_{\rm h}/M_\odot = 11.3$, near the median mass of our sample. The stellar feedback recipe includes thermal energy from supernovae, shocked stellar winds, and radiation pressure. Full details can be found in Trujillo-Gomez et al. (2013).

For this simulated galaxy, we computed the gas mass in solar masses per unit kpc per unit velocity [km s^{-1}] as a function of radial velocity and galactocentric radius and present the results in Figure 11. The dotted vertical line provides the location of the virial radius and the solid curves provide the circular velocity and the escape velocity as a function of galactocentric distance. Outflowing material (positive velocities) is seen to have radial velocities exceeding the escape velocity, whereas inflowing material (negative velocities) is always infalling with radial velocities roughly a factor of $\simeq$1.4 smaller than the escape velocity at all galactocentric radii. Outside the virial radius, the infall kinematics reflect the circular velocity, whereas inside the virial radius, the infall velocity increases relative to the circular velocity toward smaller galactocentric distances. Qualitatively identical results are found for all of the various stellar feedback models developed by Trujillo-Gomez et al. (2013), indicating that the infall kinematic behavior is independent of stellar feedback model (see Trujillo-Gomez et al. 2014).

If the absorbers in our sample are associated with the identified host galaxies, we can thus infer that clouds with velocities greater than the escape velocity are entrained in outflowing material. If so, our data, as presented in Figure 8, suggest that clouds constrained to reside outside the virial radius have a higher escape fraction than those that are not constrained to reside outside the virial radius.

5.4. *Implications of Differential Kinematics*

Having argued that the absorbing clouds in our sample are best interpreted as residing within $R \simeq 4R_{\rm vir}$ of their galaxies and that those clouds with $|v| > v_{\rm esc}$ are outflowing from the galaxy, we now explore the implications for galaxy evolution in light of our finding of differential kinematics (see Section 4.4).

By differential kinematics, we are referring to the result in which we find that the lower mass subsample has a smaller fraction of bound clouds than the higher mass subsample and, for all masses, the bound fraction decreases as $D/R_{\rm vir}$ increases. Summarizing, dividing the sample into lower mass and higher mass halos, we find that for $D/R_{\rm vir} < 1$, lower mass halos have an escape fraction of $\sim$65%, whereas higher mass halos have an escape fraction of $\sim$5%.

One highly simplified yet possible explanation for the observed trends in the data is that, the higher the launch velocity of a wind cloud, the further from the galaxy it can potentially travel (assuming the cloud destruction timescale is longer than the dynamical time). Since clouds with launch velocities below $v_{\rm esc}$ cannot achieve a distance greater than their turn-around radius, as we probe further out from the galaxy, we would naturally find that the fraction of higher velocity clouds increases.

For our higher mass subsample, $11.5 < \log(M_{\rm h}/M_\odot) \leq 12.2$, we note that the bound fractions for both H I and O VI absorbing clouds are consistent with the findings of COS-Halos (Tumlinson et al. 2011, 2013). However for our lower mass subsample, $10.8 \leq \log(M_{\rm h}/M_\odot) < 11.5$, we find higher escape fractions, and this holds for all $D/R_{\rm vir}$ bins. *This implies that galaxies with halo masses of* $\log(M_{\rm h}/M_\odot) < 11.5$ *expel a larger portion of their winds to the IGM than do higher mass galaxies. It also implies that wind recycling would characteristically be more common in higher mass galaxies than in lower mass galaxies.*

Thus, our result of differential kinematics has implications for the recycling of wind material as a function of halo mass, and in fact, is consistent with the "differential wind recycling" scenario proposed by Oppenheimer et al. (2010). Wind recycling serves as a third mechanism, in addition to "cold" and "hot" mode accretion (e.g., Kereš et al. 2005; Dekel & Birnboim 2006), for gas accretion into the ISM for fueling star formation. In the differential wind recycling scenario, the wind recycling time decreases with increasing halo mass, flattening toward the highest masses. Towards lower halo mass, the recycling time exceeds the Hubble time, so that lower mass galaxies would not experience wind recycling but have their star formation fueled primarily through cold mode

accretion. That is, the higher the halo mass, the shorter the recycling time of the wind material, where recycling time is the sum of the time in the wind, the time infalling back into the ISM, and the time before the gas is incorporated into stars or expelled (again) from the ISM. An important factor in this behavior of winds is the higher efficiency of hydrodynamic deceleration of the wind in higher mass galaxies due to their larger reservoir of CGM gas and higher overdensity environments (Oppenheimer & Davé 2008).

If differential kinematics is an observational signature of differential wind recycling in real galaxies, it would provide direct evidence supporting the findings of Oppenheimer et al. (2010) that the shape of the low mass end of the galaxy stellar mass function is governed primarily by a decrease in wind recycling as halo mass decreases.

Differential kinematics would then also provide insights into the mass-metallicity relationship of galaxies (Tremonti et al. 2004). If the ISM of lower mass halos is supplied primarily via cold-mode accretion, then the ISM of lower mass galaxies will have lower metallicity. On the other hand, differential kinematics implies that the higher mass galaxies re-accrete their enriched gas, such that the ISM enrichment of higher mass galaxies will be higher. The idea that outflows must be more efficient at removing metals from low-mass galaxies is required in order for models to reproduce the observed mass-metallicity relation has also been argued (with far more sophistication) by several others (e.g., Dalcanton 2007; Finlator & Davé 2008; Peeples & Shankar 2011).

Additional observations to better characterize differential kinematics in the CGM would be highly useful for constraining such models and increasing our understanding of the stellar mass function and mass-metallicity relationship.

5.5. *Comparing to Wind Models*

Here, we undertake an exercise to estimate the degree to which the realization of the data from our sample may be consistent with simple wind models. We investigate three constant-velocity wind models using the Monte Carlo technique. We employ the two-dimensional distribution of data presented in Figure 9. i.e., $|\Delta v|/v_{\rm esc}$ vs. $M_{\rm h}$, to constrain whether the models are statistically inconsistent or are not inconsistent with the realization of our data. Our aim is to determine the degree to which the paucity of data points with $|v(\rm los)|/v_{\rm esc} > 1$ at higher halo mass and with $|v(\rm los)|/v_{\rm esc} < 1$ at lower halo mass may be a chance realization for constant velocity wind models (those not based upon differential kinematics).

The three different wind models we investigate are: (1) a constant outflow wind velocity, $v_{\rm w}$, independent of galaxy halo mass, (2) a random wind velocity ranging from 0 km s^{-1} to a maximum velocity, $v_{\rm w}$, also independent of galaxy halo mass, and (3) the *vzw* wind model of Oppenheimer et al. (2010), in which the wind velocity scales with the stellar velocity dispersion $\sigma_*(r)$, where r is the radius at which the winds are launched. The *vzw* wind model is therefore halo mass dependent.

The model is one dimensional in which the wind velocities are plane-parallel and randomly oriented at some angle, θ, with respect to the observer's line of sight. There is significant uncertainty concerning the orientation of galactic winds with respect to galaxy inclination and position angle (i.e. orientation on the sky). Therefore, we adopt this simple model using an unweighted distribution of random angles in hopes of capturing the stochastic effects of varying galactic outflow conditions without introducing extra free parameters and/or possible model biases.

For the first two models, we varied $v_{\rm w}$ over the range 100 to 1500 km s^{-1}. For the *vzw* model (also known as " momentum driven winds"), the wind velocity is given by

$$v_{\rm w} = 3\,\sigma_*(r)\,\sqrt{f_{\rm L}-1}, \tag{3}$$

where $f_{\rm L}$ is the luminosity factor. Following Oppenheimer et al. (2010), we adopt $f_{\rm L} = 2$. The stellar velocity dispersion at the radius where the winds are launched is given by

$$\sigma_*(r) = \sqrt{-\frac{1}{2}\Phi(r)}, \tag{4}$$

where $\Phi(r)$ is the gravitational potential evaluated at the wind launch radius. We assume an NFW profile for which

$$\Phi(r) = -4\pi G\rho_0 r_s^2\,\frac{\ln(1+r/r_s)}{r/r_s}, \tag{5}$$

where r_s is the scale radius, and ρ_0 is given by

$$\rho_0 = \frac{M(R_{\rm vir})}{4\pi r_s^3[\ln(1+c)-c/(1+c)]}, \tag{6}$$

where c is the concentration parameter. Note that $M(R_{\rm vir})$ corresponds to our measurement $M_{\rm h}$. The concentration parameter is both halo mass and redshift dependent; for this exercise, we adopt the median redshift of the sample, $z = 0.21$.

For each wind in the Monte Carlo simulation, we first generate an associated galaxy halo mass, M_h, in the range of the sample galaxies, $10.8 < \log(M_h/M_\odot) < 12.2$, from which we compute the virial radius $R_{\rm vir}$. We then generate a wind orientation in the range $0^\circ < \theta < 90^\circ$ and an impact parameter in the range $57 < D < 292$ kpc (the range of the sample). We then compute the escape velocity at the galactocentric distance equal to the impact parameter D, reproducing the $v_{\rm esc}$ employed for Figure 9. For the constant velocity wind model, we assign a value to $v_{\rm w}$. For the random velocity model, we assign a maximum value of $v_{\rm w}$ and then multiply by a random $U(0,1)$ deviate. In the case of the momentum-driven *vzw* wind model, we specify the launch radius of the wind and compute $v_{\rm w}$ from Equation 3. Finally, we determine the line of sight "observed" velocity $|v(\rm los)| = v_{\rm w}\cdot\cos(\theta)$, from which we compute the ratio $|v(\rm los)|/v_{\rm esc}$.

For a given wind model, we generate 100,000 realizations (galaxy/wind pairs). From these pairs, we randomly draw 41 galaxy/wind pairs but enforce that the 41 pairs match the number of data points on Figure 9 with $D/R_{\rm vir} \le 1$, $1 < D/R_{\rm vir} \le 2$, $2 < D/R_{\rm vir} \le 3$ in each of four equally spaced halo mass bins over the range $10.8 \le \log M_{\rm h}/M_\odot \le 12.2$. Thus, the two-dimensional distribution of halo mass and $D/R_{\rm vir}$ of the 41 galaxy/wind pairs emulates that of the observed data on Figure 9. On the $|v(\rm los)|/v_{\rm esc}$–$M_{\rm h}$ plane, we then compute the two-dimensional KS statistic between the galaxy/wind pairs and the data points in order to quantify the degree to which the distribution of wind model points is inconsistent with the distribution of observed points. We adopt the criterion that the model points are inconsistent with the data when $P(\rm KS) \le 0.0027$, corresponding to a 99.97% (3 σ) or higher confidence level.

We repeat the entire process for 100,000 trials, each time calculating the two-dimensional KS probability comparing the model data to the observed data. Finally, we compute the

fraction of model trials for which $P(\mathrm{KS}) \leq 0.0027$ (i.e., the fraction out of 100,000 for which the model data can be ruled inconsistent with the observed data at the 3 σ level). As this fraction, $f(P_{\mathrm{KS}} < 0.0027)$, approaches unity, the wind model is less consistent with the data.

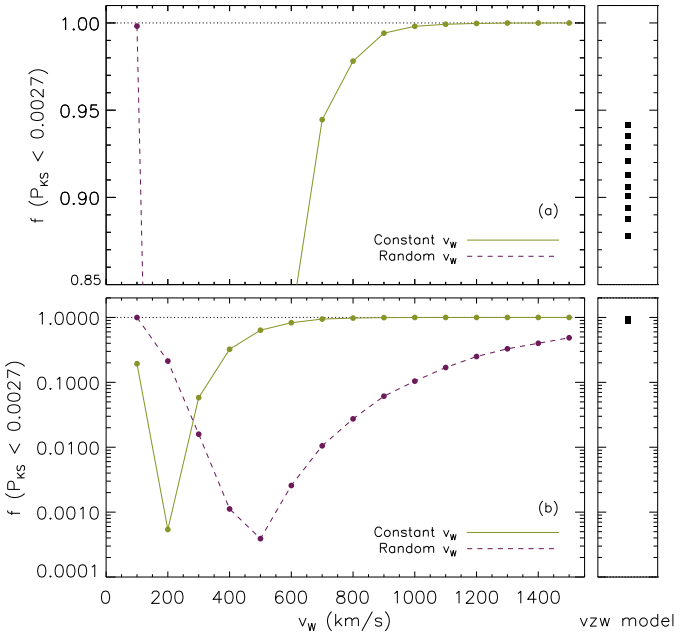

Figure 12. The fraction of realizations, $f(P_{\mathrm{KS}} < 0.0027)$, that are inconsistent with the data at the 3 σ level versus the wind velocity, v_{w}, for three different wind models. Panel (a) shows a linearly scaled zoom-in of the upper region of panel (b). For the constant wind velocity model, v_{w} is the wind velocity. For the random wind velocity model, v_{w} is the maximum wind velocity, which can range from 0 km s^{-1} to v_{w}. The *vzw* wind model (right panels) is computed for wind launch radii over the range r = 1–10 kpc in steps of 1 kpc. The upper point corresponds to r = 1 kpc and the lower point corresponds to r = 10 kpc. The random wind models with wind velocities peaking around $\sim$ 500 km s^{-1} are most frequently consistent with the data.

In Figures 12(a) and 12(b), we plot $f(P_{\mathrm{KS}} < 0.0027)$ as a function of v_{w} for the constant velocity and random velocity wind models. For the random wind model, v_{w} represents the maximum value of the constant velocity wind. Panel (a) is a linearly scaled zoom-in of the upper portion of panel (b). Where the curves have $f(P_{\mathrm{KS}} < 0.0027) \geq 0.9$, the distribution of the model data is ruled out at the 3 σ level for 90% or more of the realizations. The right-hand panels show $f(P_{\mathrm{KS}} < 0.0027)$ for the *vzw* wind model for ten different launch radii ranging from r = 1 to 10 kpc in steps of 1 kpc. For this model, the value of $f(P_{\mathrm{KS}} < 0.0027)$ increases as the launch radius decreases (the highest $f(P_{\mathrm{KS}} < 0.0027)$ corresponds to r = 1 kpc).

For the constant velocity wind model, $f(P_{\mathrm{KS}} < 0.0027) \geq 0.9$ occurs for $v_{\mathrm{w}} \geq 650$ km s^{-1}. That the range of velocities below this value is less frequently inconsistent with the data is not outside of expectations, since 90% of the H I absorbing cloud velocities lie within $\Delta v = \pm 500$ km s^{-1}. Note that it is very rare for the realizations to be inconsistent with the data for $v_{\mathrm{w}} \simeq 200$ km s^{-1}, the value within which 70% of all H I absorbing cloud velocity offsets lie with respect to the galaxy.

For the random velocity wind model, $f(P_{\mathrm{KS}} < 0.0027) \geq 0.9$ occurs for $v_{\mathrm{w}} \simeq 100$ km s^{-1}. Recall that in this model, the wind velocity of any given galaxy/wind pair falls in the range 0 km s^{-1} to the maximum velocity, v_{w}. We find $f(P_{\mathrm{KS}} < 0.0027) < 0.9$ occurs for all wind velocities $v_{\mathrm{w}} > 100$ km s^{-1}, indicating that the random velocity wind model cannot be ruled as being inconsistent with the data for more than 90% of the realizations over the range $100 < v_{\mathrm{w}} \leq 1500$ km s^{-1}.

For the *vzw* wind model, $f(P_{\mathrm{KS}} < 0.0027) \geq 0.90$ occurs for launch radii $r \leq 5$ kpc. Formally, the *vzw* wind model cannot be ruled as inconsistent with the data; however, for reasonably physical launch radii, 90% of the realizations are inconsistent with the data to the 3 σ level. Generally, the *vzw* wind model does not exhibit a compelling signature for being consistent with the data.

That the random velocity wind model can be consistent with the data suggests that, even in a small sample (14 galaxies with 41 absorbing clouds), highly variable wind velocities from galaxy to galaxy can give rise to the differential kinematics we inferred from the data. This remains consistent with our previous statement that one possible explanation for differential kinematics is that (in real galaxies) the higher the launch velocity of the wind, the further from the galaxy the absorbing clouds potentially travel, so that as we probe further out from a galaxy we observe a higher fraction of higher velocity clouds.

If the cloud velocities are decelerated dynamically in higher mass galaxies, as found in the simulations of Oppenheimer et al. (2010), then higher wind velocities would be more frequently observed in the outer extended CGM of lower mass galaxies, as we have inferred for our sample. In the wind model of Chelouche & Bowen (2010), the wind velocity is proportional to the star formation rate in the galaxy disk. We do not have estimates of the star formation rates for the galaxies in our sample. But, we note that variations in the star formation rate from galaxy to galaxy would manifest in their model in a manner similar to our random velocity wind model. We also note, generally, that lower (stellar) mass galaxies tend to have higher specific star formation rates than higher mass galaxies (cf., Schawinski et al. 2014), and it seems reasonable that specific star formation rate would correlate with wind velocity.

6. CONCLUSIONS

We have presented an analysis of the spatial and geometric distribution and kinematics of H I and O VI absorption surrounding 14 galaxies within a projected distance of D = 300 kpc of background quasars. The galaxies are imaged using *HST*/WFPC2 and their morphological and orientation parameters have been measured using GIM2D. The absorption is measured in *HST*/COS or *HST*/STIS quasar spectra. We have focused our analysis on the Lyα and Lyβ transitions, and O VI $\lambda\lambda$1031, 1037 doublet. The column densities, number of clouds, and the kinematics were measured using Voigt profile fitting.

The sample is characterized by a redshift range $0.12 \leq z \leq 0.67$, and an impact parameter range $60 \leq D \leq 290$ kpc. The galaxy virial masses range from $10.8 \leq \log(M_{\mathrm{h}}/M_{\odot}) \leq 12.2$, corresponding to virial radii between $70 \leq R_{\mathrm{vir}} \leq 225$ kpc. The median virial mass is $\log(M_{\mathrm{h}}/M_{\odot}) = 11.5$. The range of D/R_{vir} spans from 0.45 to 2.75. The range of galaxy inclinations and azimuthal angles are $18^{\circ} \leq i \leq 85^{\circ}$ and $6^{\circ} \leq \Phi \leq 87^{\circ}$, respectively.

6.1. *Spatial and Geometric Distributions*

We first highlight some general results with regards to the spatial and geometric distribution of H I and O VI absorbing

gas in the CGM.

1. Although higher N(H I) systems are found at $D <$ 100 kpc, there is no statistical trend between N(H I) and D. Over the range $100 \leq D \leq 300$ kpc, the system total N(H I) is typically $\log N(\mathrm{H\,I}) \simeq 14$. For all D, the mean and dispersion is $\log\langle N(\mathrm{H\,I})\rangle = 14.34 \pm 0.61$. We detect O VI as far as $D \sim 290$ kpc (our sample maximum), to a 3 σ limit of $\log N(\mathrm{O\,VI}) = 12.8$. The distribution of N(O VI) is effectively flat as a function of D, showing no statistically significant trend between N(O VI) and projected distance from the host galaxy. The mean and dispersion is $\log\langle N(\mathrm{O\,VI})\rangle = 14.03 \pm 0.44$.

2. There is a higher average value and a broader spread in N(H I) for $D/R_{\rm vir} < 1$ as compared to $D/R_{\rm vir} > 1$, with $\log\langle N(\mathrm{H\,I})\rangle = 15.9 \pm 1.6$ inside and $\log\langle N(\mathrm{H\,I})\rangle = 14.1 \pm 0.5$ outside the projected virial radius, respectively. Due to the flat spatial distribution of N(O VI) with D and the higher average value and dispersion of N(H I) at $D/R_{\rm vir} < 1$, the dispersion in $N(\mathrm{O\,VI})/N(\mathrm{H\,I})$ is a factor of $\simeq 8$ greater inside the projected virial radius.

3. The is no discernible trend between the system total N(H I), N(O VI), or $N(\mathrm{O\,VI})/N(\mathrm{H\,I})$ and galaxy inclination. Statistically, there is no correlation between these quantities and azimuthal angle. However, in our small sample, N(H I) is largest when probed nearest to the project axes of the galaxy and decreases as the azimuthal angle increases away from the projected axes.

4. Within $D = 300$ kpc, there is a higher incidence of O VI absorption in higher mass halos than in lower mass halos, using the sample median of $\log M_{\rm h}/M_{\odot} = 11.5$ to divide the masses into "higher" and "lower". We find associated O VI absorption in only $\sim 40\%$ of the H I clouds in and around lower mass halos as compared to $\sim 85\%$ around higher mass halos. Since the system total N(H I) is fairly flat, the smaller fraction of detected O VI clouds in lower mass halos suggest conditions favoring O VI is less common out to $D = 300$ kpc of lower mass halos than for higher mass halos, but that the physical conditions of the gas are not dissimilar.

In summary, the highest N(H I) clouds reside within the projected virial radius and are found at azimuthal angles closely aligned with the galaxy projected axes. It could be that for $D/R_{\rm vir} < 1$, the H I in our sample is reflecting the presence of a cool/warm gas phase preferentially found along the projected galaxy axes, such is observed for Mg II absorption (Bordoloi et al. 2011; Kacprzak et al. 2012a; Bouché et al. 2012). The data we have in hand cannot definitively address the presence of a cool/warm phase. Overall, it appears that there is a transition in the behavior of H I absorption in the regime of $D/R_{\rm vir} \sim 1$, in which higher system total N(H I) is found inside the projected virial radius and $\log N(\mathrm{H\,I}) \simeq 14$ outside the projected virial radius at least as far as $D/R_{\rm vir} \simeq 3$. For O VI absorption, the distribution of the system total N(O VI) is flat for all $D/R_{\rm vir}$ out to at least $D/R_{\rm vir} \sim 2.8$. O VI absorbers are more common in the CGM of higher mass halos out to $D \simeq 300$ kpc. Altogether, N(O VI) shows no preferred geometric dependencies, suggesting that regions of hot CGM gas are quite globally distributed.

6.2. *Differential Kinematics*

The main result of this paper is differential behavior in the fraction of bound clouds (individual VP components) as a function of both virial mass, $M_{\rm h}$, and virial radius, $R_{\rm vir}$. We called this behavior "differential kinematics". These findings are shown in Figure 9 and Table 4. Figure 9 shows the absolute relative velocity of the Voigt profile "cloud" velocities with respect to the galaxy normalized to the escape velocity, $|\Delta v/v_{\rm esc}|$, as a function of virial and stellar mass, $M_{\rm h}$ and M_*. Table 4 lists the fraction of clouds that can be inferred to be bound to the host halo as a function of $M_{\rm h}$ and $D/R_{\rm vir}$. The interpretation relies heavily upon the inference (presented in Section 5.3) that clouds with $|\Delta v/v_{\rm esc}| > 1$ are most probably outflowing through the CGM, and are not IGM Hubble flow or infalling CGM or IGM clouds. We highlight the results from our kinematic analysis.

1. Most H I and O VI absorbing clouds are clustered within ~ 500 km s^{-1}. In $\sim 50\%$ of the systems with detected O VI absorption, we observe a velocity offset between the bulk of the H I and the bulk of the O VI, as defined by the highest column density Voigt profile components in a system. In three of these cases, the velocity offset is ~ 100 km s^{-1}. The data support the idea that the $\log N(\mathrm{H\,I}) \simeq 14$ regime of the CGM represents various gas conditions as inferred from H I and O VI absorption, even though the system *total* N(H I), N(O VI), and $N(\mathrm{O\,VI})/N(\mathrm{H\,I})$ show little variation from system to system.

2. When the full range of $M_{\rm h}$ and $D/R_{\rm vir}$ of the sample are examined, $\sim 40\%$ of the H I absorbing clouds can be inferred to be escaping their host halo. Segregating the sample into finite ranges of $D/R_{\rm vir}$, the fraction of bound clouds decreases as $D/R_{\rm vir}$ increases such that the escaping fraction is $\sim 15\%$ for $D/R_{\rm vir} < 1$, $\sim 45\%$ for $1 \leq D/R_{\rm vir} < 2$, and $\sim 90\%$ for $2 \leq D/R_{\rm vir} < 3$. That is, averaged over all $M_{\rm h}$, the fraction of H I absorbing clouds that could be escaping the galaxy increases with increasing $D/R_{\rm vir}$.

3. Dividing the sample into lower mass and higher mass halos, where the dividing virial mass is the median of the sample, $\log M_{\rm h}/M_{\odot} = 11.5$, we find that the lower mass subsample has a smaller fraction of bound clouds in each of the three aforementioned $D/R_{\rm vir}$ ranges. For $D/R_{\rm vir} < 1$, lower mass halos have an escape fraction of $\sim 65\%$, whereas higher mass halos have an escape fraction of $\sim 5\%$. For $1 \leq D/R_{\rm vir} < 2$, the escape fractions are $\sim 55\%$ and $\sim 35\%$ for lower mass and higher mass halos, respectively. For $2 \leq D/R_{\rm vir} < 3$, the escape fraction for lower mass halos is $\sim 90\%$ (higher mass halos were not probed in this range in our sample).

4. We demonstrated that the absorbing clouds are likely to be outflowing winds, since their kinematics are not consistent with infall kinematics, based upon feedback simulations. We showed that the absorbing gas is likely to reside within $4R_{\rm vir}$ of the galaxies, also based upon simulations and the dynamics of Hubble flow. We explored three constant velocity wind models to explore the degree to which the observed characteristics of differential kinematics are inconsistent with these models. We find that the most consistent constant wind velocity model is that with random winds velocities in the range $300 \leq v_{\rm w} \leq 800$ km s^{-1}, and suggest that specific star formation rate, from galaxy to galaxy, coupled with higher dynamical deceleration of the gas in higher mass halos, may be instrumental in explaining differential kinematics.

Differential kinematics may be an observational signature supporting the theoretical scenario of differential wind recycling proposed by Oppenheimer et al. (2010). If so, differential kinematics would be an important finding that should be verified and further characterized with additional observations. It is becoming well accepted that wind recycling through the CGM is an important regulating process for galaxy evolution and may, to a large degree, control the shape of the stellar to halo mass function and the mass-metallicity

relationship of galaxies.

We thank Ben Oppenheimer for helpful and insightful discussions on the details of his wind simulations. NLM, CWC, and SM were supported mainly through grant HST-GO-13398 and JCC and SM were partially supported by grant HST-AR-12644, both provided by NASA through the Space Telescope Science Institute, which is operated by the Association of Universities for Research in Astronomy (AURA) under NASA contract NAS 5-26555. ST-G was supported through the Research Enhancement Program awarded to CWC provided by NASA's New Mexico Space Grant Consortium (NMSGC). NLM and NMN were partially supported through NMSGC Graduate Research Fellowships. NMN was also partially supported through a three-year Graduate Research Enhancement Grant (GREG) sponsored by the Office of the Vice President for Research at New Mexico State University.

APPENDIX

A. INDIVIDUAL QUASAR FIELDS

All spectroscopic redshift data for the galaxies analyzed in this paper come from one of five different sources. (1) Very early work was conducted by Ellingson & Yee (1994), who employed the MARLIN/LAMA Multiobject Spectrograph on the Canada-France-Hawaii Telescope (CFHT). They cite a 78% completeness level for successful spectroscopic identification of observed galaxies with $m_r \leq 21.5$, and 49% for the fields overall. (2) A survey by Lanzetta et al. (1995) uses the Kast Spectrograph on the Lick Observatory 3-m telescope. This study is 37% complete for $m_r < 21.5$, with limiting magnitudes of m_r = 23.0 and m_r = 23.5 for the fields toward Q1001+2910 and Q1704+6048, respectively. This survey adopted some of the galaxy identifications from Ellingson & Yee (1994). (3) A survey by Le Brun et al. (1996) was conducted with the MOS multi-slit spectrograph on the CFHT. They they claim a success rate of 81% for all observed galaxies to a limiting magnitude of m_r = 22.5. (4) An *HST* imaging survey, using FOS quasar spectroscopy, was conducted by Chen et al. (1998, 2001), targeting the fields studied by Lanzetta et al. (1995) and additional fields for which much of the details are to appear in Chen et al. (2001, in preparation). Estimates on the completeness and magnitude limits for quasar fields using only these observations will be made from published data on a field-by-field basis below. Finally, (5), Johnson et al. (2013), performed detailed spectroscopic follow-up observations of the galaxies in the field of Q0405–123. Their study employed IMACS and LDSS3 on Magellan and DIS on the Apache Point 3.5-m telescope. They cite a 100% completeness level for $L > 0.1L_*$ galaxies at impact parameters less than 100 kpc and a 75% completeness level for $L > 0.1L_*$ galaxies at impact parameters less than 500 kpc.

Galaxy and absorber data can be found in Tables 2 and 3, respectively. Galaxy image footprints and analyzed spectra for Lyα, Lyβ, and O VI $\lambda\lambda$1031, 1037 profiles are show in Figure 1 in Section 3 and here in Figures A1–A4.

A.1. *The Field Toward Q0405–123*

This field was first spectroscopically surveyed by Ellingson & Yee (1994) and has had follow-up observations published in Johnson et al. (2013). Nearly all of the redshifts measured by Ellingson & Yee (1994) have been revised. Some galaxies associated with absorbers in Chen et al. (2001), which uses the Ellingson redshifts, have changed significantly. The galaxy measured at $z_{\rm gal}$ = 0.3520 was revised to $z_{\rm gal}$ = 0.3422 and a galaxy located off the WFPC2 image footprint was identified at $z_{\rm gal}$ = 0.3521. The galaxy originally measured at $z_{\rm gal}$ = 0.2800 was revised to $z_{\rm gal}$ = 0.7115 and a new galaxy at $z_{\rm gal}$ = 0.4100 was added to the field. There are a large number of galaxies clustered both spatially and in redshift space at $z_{\rm QSO}$ = 0.57 that are not considered in this study due to their likely physical connection to the quasar. In addition, there are four galaxy pairs whose absorption cannot be disentangled (the first at $z_{\rm gal}$ = 0.1669 and $z_{\rm gal}$ = 0.1672, the second at $z_{\rm gal}$ = 0.5169 and $z_{\rm gal}$ = 0.5161, the third at $z_{\rm gal}$ = 0.3422 and $z_{\rm gal}$ = 0.3407, and the fourth at $z_{\rm gal}$ = 0.3614 and $z_{\rm gal}$ = 0.3608). We exclude these galaxies from our analysis.

We examine galaxy-absorber pairs at redshifts $z_{\rm gal}$ = 0.1534, 0.2978, and 0.4100.

A.2. *The Field Toward Q0454–2203*

The galaxy identifications come from Chen et al. (1998), but the spectroscopic survey of the field remains unpublished. From Chen et al. (1998), we estimate that the survey limiting magnitude is $m_r \sim 21.8$. There are two galaxies in the field within $\sim$300 km s^{-1} of each other ($z_{\rm gal}$ = 0.4837 and $z_{\rm gal}$ = 0.4847) that are not included in our study (they also do not have UV spectra covering Lyα, Lyβ, and O VI).

We examine only the galaxy-absorber pair for the galaxy at $z_{\rm gal}$ = 0.3818.

A.3. *The Field Toward Q1001+2910*

This field was spectroscopically surveyed by Lanzetta et al. (1995). There are only a few bright galaxies near the quasar, allowing straight-forward identification of galaxy-absorber pairs. We note that the galaxy at $z_{\rm gal}$ = 0.2143 does not appear in Chen et al. (1998), but does appear in Chen et al. (2001) with no elaboration. We adopt the Chen et al. (2001) data.

We examine galaxy-absorber pairs at redshifts $z_{\rm gal}$ = 0.1380 and 0.2143.

A.4. *The Field Toward Q1136–1334*

As with the Q0454–2203 field, the galaxy identifications come from Chen et al. (1998), but the detailed spectroscopic survey of the field remains unpublished. From Chen et al. (1998), we estimate that the survey limiting magnitude is $m_r \sim 22.3$. There are three galaxies clustered around $z_{\rm gal} \simeq 0.36$ which are excluded from our study due also to a lack of UV spectral coverage of Lyα, Lyβ, and O VI absorption in the COS spectrum.

We examine galaxy-absorber pairs at redshifts $z_{\rm gal}$ = 0.1755 and 0.2044.

A.5. *The Field Toward Q1216+0655*

The galaxy identifications come from Chen et al. (2001), but the detailed spectroscopic survey of the field remains unpublished. From Chen et al. (2001), we estimate that the survey limiting magnitude is $m_r \sim 21.6$. There is only one galaxy identified that has a redshift lower than that of the quasar with the required spectral coverage in the COS spectrum.

We examine the only galaxy-absorber pair at redshift $z_{\rm gal}$ = 0.1242.

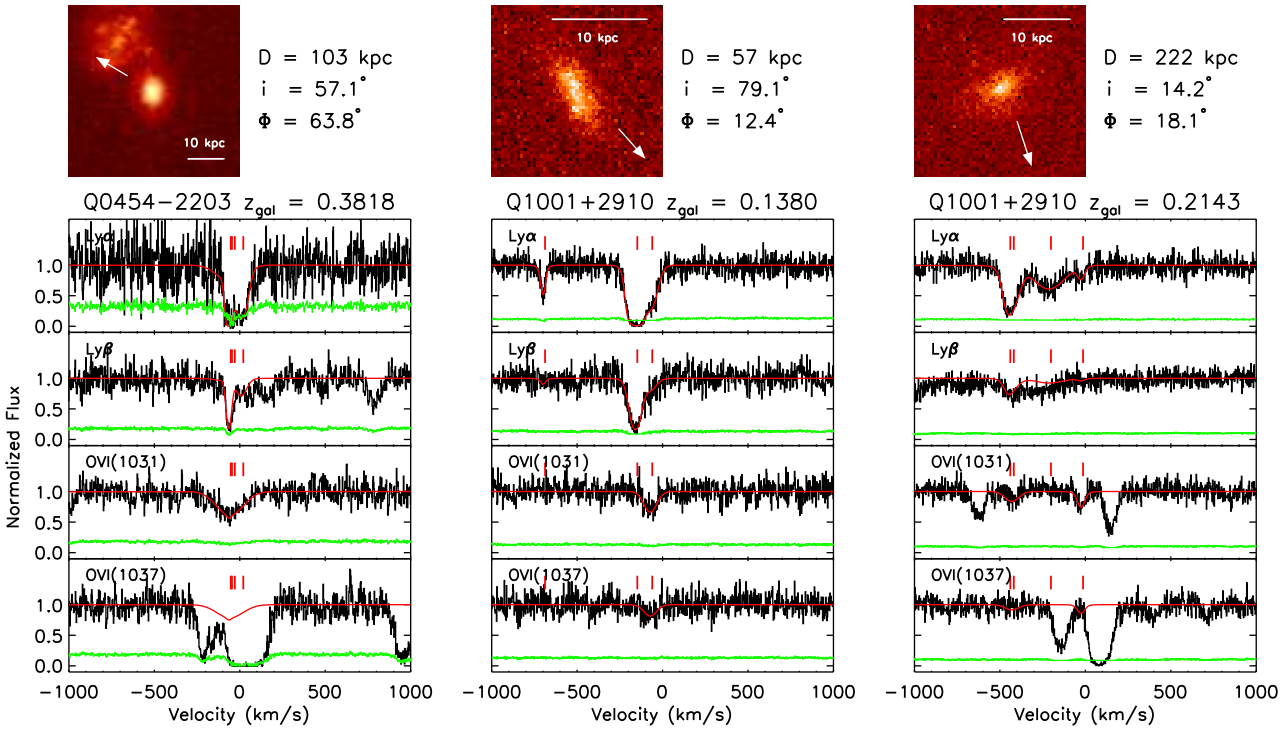

Figure A1. Same as Figure 1, but for the galaxy at z_{gal} = 0.3818 in the field toward Q0454–2203, and the galaxies at z_{gal} = 0.1380 and z_{gal} = 0.2143 in the field toward Q1001+2910.

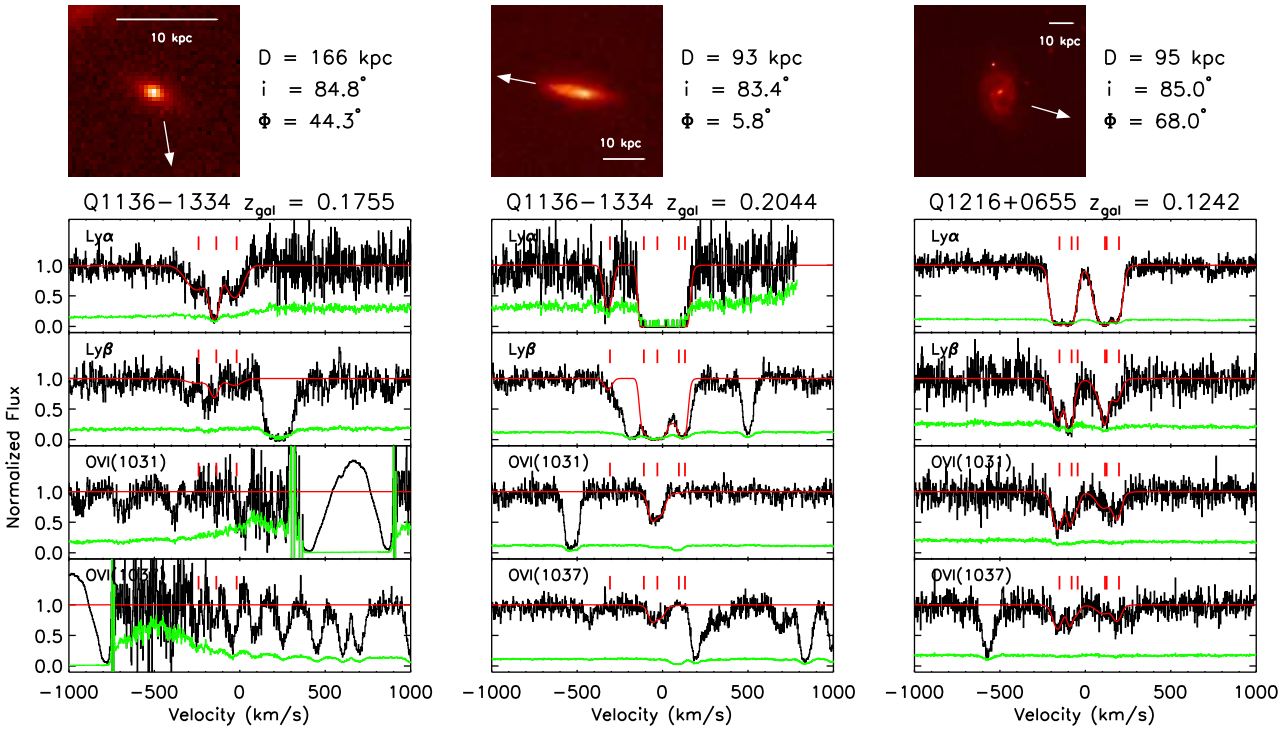

Figure A2. Same as Figure 1, but for the galaxies at z_{gal} = 0.1755 and z_{gal} = 0.2044 in the field toward Q1136–1334, and the galaxy at z_{gal} = 0.1242 in the field toward Q1216+0655.

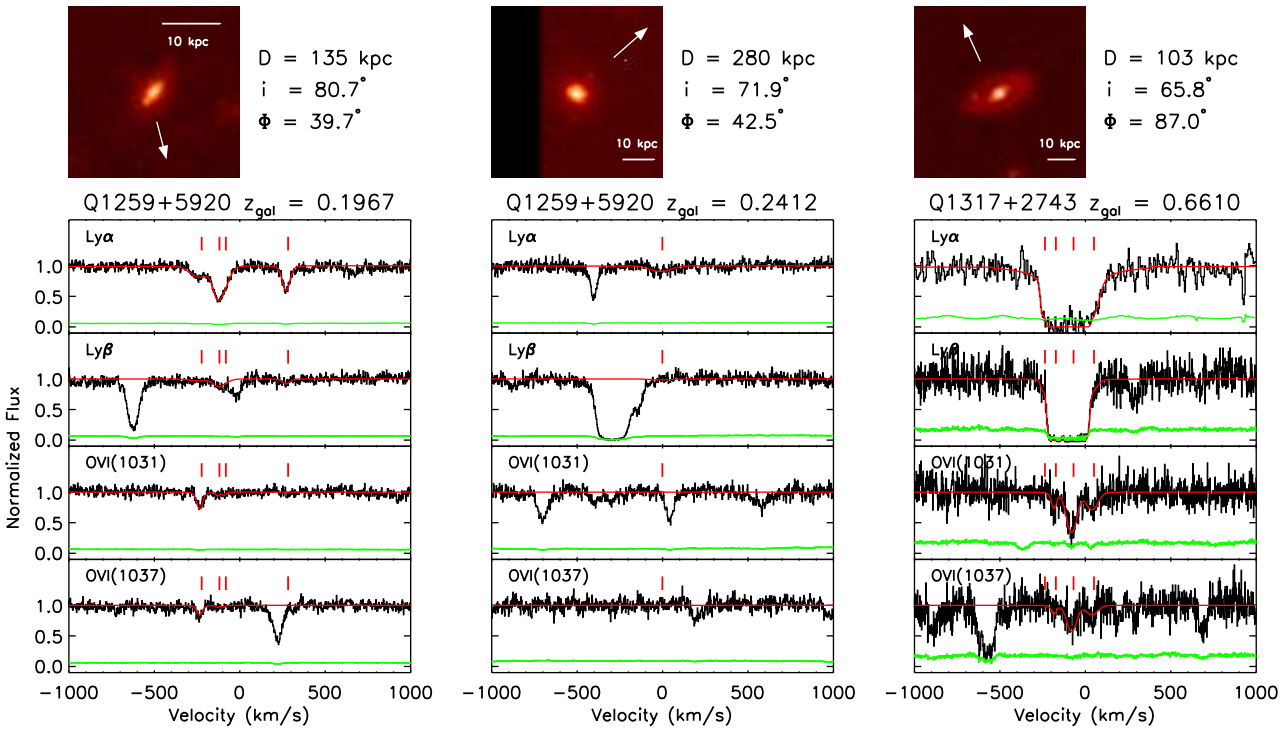

Figure A3. Same as Figure 1, but for the galaxies at z_{gal} = 0.1967 and z_{gal} = 0.2412 in the field toward Q1259+5920, and the galaxy at z_{gal} = 0.6610 in the field toward Q1317+2743.

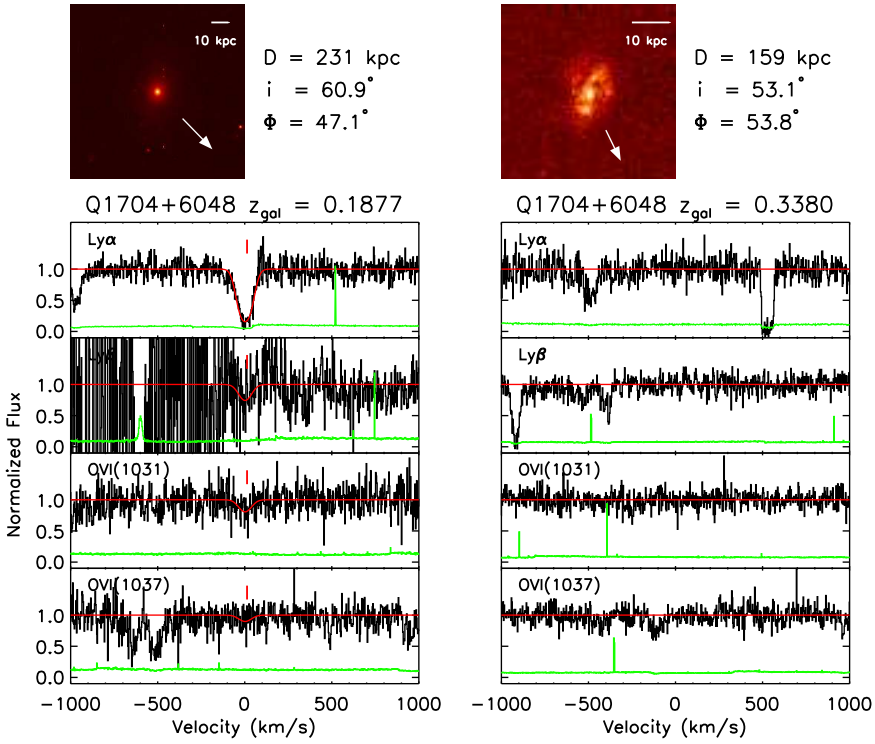

Figure A4. Same as Figure 1, but for the galaxies at z_{gal} = 0.1877 and z_{gal} = 0.3380 in the field toward Q1704+6048.

A.6. *The Field Toward Q1259+5920*

The galaxy identifications come from Chen et al. (2001), but the detailed spectroscopic survey of the field remains unpublished. From Chen et al. (2001), we estimate that the survey limiting magnitude is $m_r \sim 21.1$.

We examine galaxy-absorber pairs at redshifts $z_{\rm gal}$ = 0.1967 and 0.2412. These two galaxies were imaged by different programs (see Table 1).

A.7. *The Field Toward Q1317+2743*

This field was spectroscopically surveyed by Le Brun et al. (1996). They report two pairs of galaxies in this field ($z_{\rm gal}$ = 0.5397 and 0.5398, and $z_{\rm gal}$ = 0.6715 and 0.6717). All absorption of interest from the $z \simeq 0.54$ galaxies falls in the gaps in the COS spectrum. Chen et al. (2001) also studied this field. The most recent work is from Churchill et al. (2012), who studied the $z_{\rm gal}$ = 0.6719 galaxy and Kacprzak et al. (2012b), who studied the $z_{\rm gal}$ = 0.6610 galaxy. These galaxy redshifts are revisions from the Le Brun et al. (1996) work.

Because of the complexity of the absorption associated with the $z_{\rm gal}$ = 0.6719 galaxy, we examine only the galaxy-absorber pair at redshift $z_{\rm gal}$ = 0.6610.

A.8. *The Field Toward Q1704+6048*

This field was spectroscopically surveyed by both Lanzetta et al. (1995) and Le Brun et al. (1996).

Ambiguity in this field exists for the galaxies identified at $z_{\rm gal}$ = 0.2260 and $z_{\rm gal}$ = 0.2217. Both galaxies are first measured and identified by Le Brun et al. (1996), but only the galaxy at $z_{\rm gal}$ = 0.2260 appears in Chen et al. (2001) because of its proximity to the quasar line of sight (D = 260 kpc). Chen et al. (2001) do not identify an absorber with the $z_{\rm gal}$ = 0.2260 galaxy. The other galaxy, with $D \sim 530$ kpc, has a redshift nearly coincident with absorber at $z_{\rm abs}$ = 0.2216. Due to the large transverse distance from the quasar and its possible ambiguity with the galaxy at $z_{\rm gal}$ = 0.2260, we do not include these galaxies in our analysis.

We examine galaxy-absorber pairs at redshifts $z_{\rm gal}$ = 0.1877 and 0.3380.

B. COLUMN DENSITIES

For this work, we present H I column densities using only the Lyα and Lyβ transitions. For roughly half of our sample the Lyγ is also available for fitting. As such, requiring Lyγ for the fits would significantly reduce our sample size.

To ensure that the Voigt profile fits using Lyα and Lyβ only are not systematically skewed relative to fits using Lyα, Lyβ, and Lyγ, we compared the fits with and without Lyγ for the subsample that has Lyγ coverage.

In Figure B1, we present the H I column densities derived from Lyα and Lyβ only fits and Lyα, Lyβ, and Lyγ fits. The resulting column densities are virtually identical for non-saturated lines. Even in the saturated higher column density lines, the resulting column densities are highly consistent with a one-to-one correlation. We thus have validated that omitting the Lyγ transition provides no skew in the resulting H I column densities.

C. DEBLENDING

In two cases, we identified absorption components blended with other absorption features from a different redshift. Here, we illustrate our deblending technique.

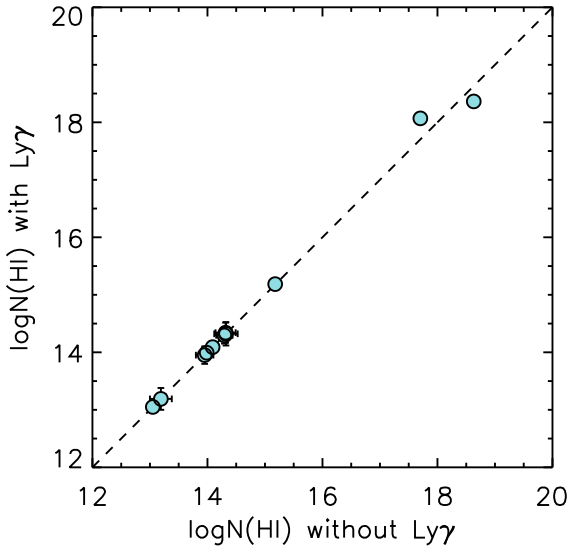

Figure B1. Voigt profile column density results for $\log N$(H I). On the x-axis is the resultant column density measured using only Lyα and Lyβ. On the y-axis is the result using Lyα, Lyβ, and Lyγ. The dotted line shows a one-to-one correlation. Including the Lyγ with the fit has very little impact on the measured H I column density.

The first case occurs in the Lyβ line associated with the $z_{\rm gal}$ = 0.4100 galaxy in the field of Q0405–123. The Lyβ is blended with N V λ1238 at $z_{\rm abs}$ = 0.1670. In Figure C1, we show the results of removing the contaminating N V λ1238 line. The red lines show the fit and data for the contaminating N V λ1238 line. In blue is the accompanying Voigt profile fit for the corresponding N V λ1243 line.

The second case occurs in the absorption associated with the galaxy in the field of Q1136–1334 at $z_{\rm gal}$ = 0.2044. Both members of the O VI $\lambda\lambda$1031, 1037 doublet suffer blending with Lyman-series absorption from two different higher-redshift absorbers (O VI λ1031 is contaminated by Lyβ at $z_{\rm abs}$ = 0.2121 and O VI λ1037 is contaminated by Lyϵ at $z_{\rm abs}$ = 0.3329). In Figure C2, we show the deblending results. Again, we highlight in red both the fits and subtracted components of the contaminating transitions (Lyβ and Lyϵ).

REFERENCES

Bahcall, J. N., Bergeron, J., Boksenberg, A., et al. 1993, ApJS, 87, 1
Behroozi, P. S., Conroy, C., & Wechsler, R. H. 2010, ApJ, 717, 379
Behroozi, P. S., Marchesini, D., Wechsler, R. H., et al. 2013, ApJ, 777, L10
Bertin, E., & Arnouts, S. 1996, A&AS, 117, 393
Birnboim, Y., & Dekel, A. 2003, MNRAS, 345, 349
Bordoloi, R., Lilly, S. J., Knobel, C., et al. 2011, ApJ, 743, 10
Bouché, N., Hohensee, W., Vargas, R., et al. 2012, MNRAS, 426, 801
Brown, T. et al. 2002, *HST* STIS Data Handbook, version 4.0, ed. B. Mobasher, (Baltimore: STScI)
Bryan, G. L., & Norman, M. L. 1998, ApJ, 495, 80
Bullock, J. S., Kolatt, T. S., Sigad, Y., et al. 2001, MNRAS, 321, 559
Chelouche, D., & Bowen, D. V. 2010, ApJ, 722, 1821
Chen, H.-W., Lanzetta, K. M., Webb, J. K., & Barcons, X. 1998, ApJ, 498, 77
—. 2001, ApJ, 559, 654
Churchill, C. W., Kacprzak, G. G., Steidel, C. C., et al. 2012, ApJ, 760, 68
Churchill, C. W., Mellon, R. R., Charlton, J. C., et al. 2000, ApJS, 130, 91
Churchill, C. W., Nielsen, N. M., Kacprzak, G. G., & Trujillo-Gomez, S. 2013a, ApJ, 763, L42
Churchill, C. W., Rigby, J. R., Charlton, J. C., & Vogt, S. S. 1999, ApJS, 120, 51
Churchill, C. W., Trujillo-Gomez, S., Nielsen, N. M., & Kacprzak, G. G. 2013b, ArXiv e-prints
Churchill, C. W., & Vogt, S. S. 2001, AJ, 122, 679

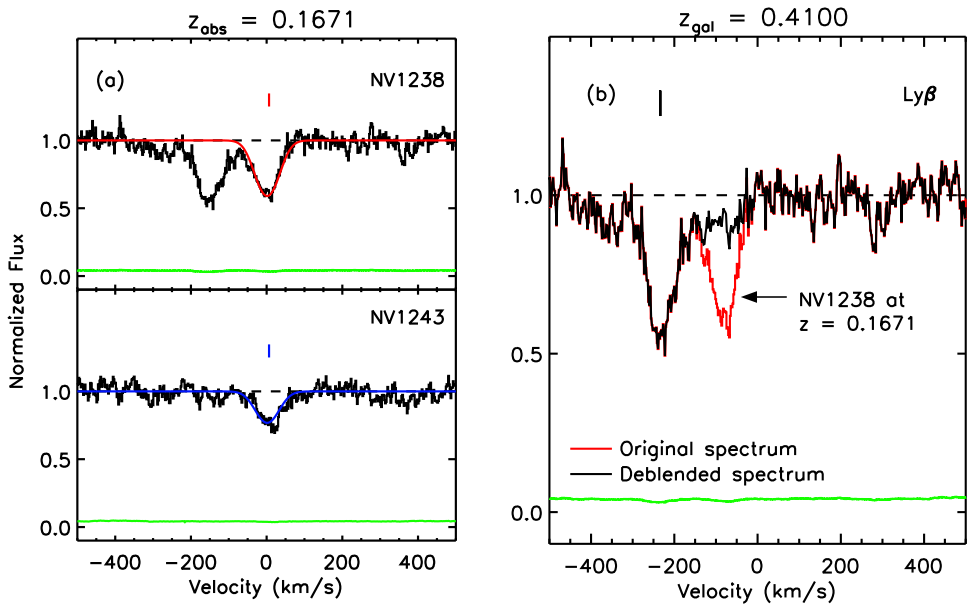

Figure C1. Deblending of Lyβ for absorption associated with the galaxy at z_{gal} = 0.4100 in the field of Q0405−123. The Lyβ line is blended with N v λ1238 at z_{abs} = 0.1671. The red spectrum is the original data and the black spectrum is the result of the deblending process.

Cooksey, K. L., Prochaska, J. X., Chen, H.-W., Mulchaey, J. S., & Weiner, B. J. 2008, ApJ, 676, 262
Cuesta, A. J., Prada, F., Klypin, A., & Moles, M. 2008, MNRAS, 389, 385
Dalcanton, J. J. 2007, ApJ, 658, 941
Danforth, C. W., & Shull, J. M. 2008, ApJ, 679, 194
Davé, R., Hernquist, L., Katz, N., & Weinberg, D. H. 1999, ApJ, 511, 521
Dekel, A., & Birnboim, Y. 2006, MNRAS, 368, 2
Ellingson, E., & Yee, H. K. C. 1994, ApJS, 92, 33
Evans, J. L. 2011, PhD thesis, New Mexico State University
Finlator, K., & Davé, R. 2008, MNRAS, 385, 2181
Ford, A. B., Oppenheimer, B. D., Davé, R., et al. 2013, MNRAS, 432, 89
Fumagalli, M., Prochaska, J. X., Kasen, D., et al. 2011, MNRAS, 418, 1796
Gehrels, N. 1986, ApJ, 303, 336
Hellsten, U., Davé, R., Hernquist, L., Weinberg, D. H., & Katz, N. 1997, ApJ, 487, 482
Johnson, S. D., Chen, H.-W., & Mulchaey, J. S. 2013, MNRAS, 434, 1765
Kacprzak, G. G., Churchill, C. W., Ceverino, D., et al. 2010, ApJ, 711, 533
Kacprzak, G. G., Churchill, C. W., Evans, J. L., Murphy, M. T., & Steidel, C. C. 2011, MNRAS, 416, 3118
Kacprzak, G. G., Churchill, C. W., & Nielsen, N. M. 2012a, ApJ, 760, L7
Kacprzak, G. G., Churchill, C. W., Steidel, C. C., Spitler, L. R., & Holtzman, J. A. 2012b, MNRAS, 427, 3029
Kereš, D., Katz, N., Fardal, M., Davé, R., & Weinberg, D. H. 2009, MNRAS, 395, 160
Kereš, D., Katz, N., Weinberg, D. H., & Davé, R. 2005, MNRAS, 363, 2
Klypin, A. A., Trujillo-Gomez, S., & Primack, J. 2011, ApJ, 740, 102
Lanzetta, K. M., Bowen, D. V., Tytler, D., & Webb, J. K. 1995, ApJ, 442, 538
Le Brun, V., Bergeron, J., & Boisse, P. 1996, A&A, 306, 691
Lehner, N., Savage, B. D., Wakker, B. P., Sembach, K. R., & Tripp, T. M. 2006, ApJS, 164, 1
Maller, A. H., & Bullock, J. S. 2004, MNRAS, 355, 694
Mo, H. J., & Miralda-Escude, J. 1996, ApJ, 469, 589
Moster, B. P., Somerville, R. S., Maulbetsch, C., et al. 2010, ApJ, 710, 903
Muzahid, S. 2014, ApJ, 784, 5
Narayanan, A., Charlton, J. C., Masiero, J. R., & Lynch, R. 2005, ApJ, 632, 92
Narayanan, A., Savage, B. D., Wakker, B. P., et al. 2011, ApJ, 730, 15
Navarro, J. F., Frenk, C. S., & White, S. D. M. 1997, ApJ, 490, 493
Nielsen, N. M., Churchill, C. W., & Kacprzak, G. G. 2013a, ApJ, 776, 115
Nielsen, N. M., Churchill, C. W., Kacprzak, G. G., & Murphy, M. T. 2013b, ApJ, 776, 114
Oppenheimer, B. D., & Davé, R. 2008, MNRAS, 387, 577
—. 2009, MNRAS, 395, 1875
Oppenheimer, B. D., Davé, R., Kereš, D., et al. 2010, MNRAS, 406, 2325
Peeples, M. S., & Shankar, F. 2011, MNRAS, 417, 2962
Prochaska, J. X., Chen, H.-W., Howk, J. C., Weiner, B. J., & Mulchaey, J. 2004, ApJ, 617, 718
Prochaska, J. X., Weiner, B., Chen, H.-W., Mulchaey, J., & Cooksey, K. 2011, ApJ, 740, 91
Richter, P., Savage, B. D., Tripp, T. M., & Sembach, K. R. 2004, ApJS, 153, 165
Rudie, G. C., Steidel, C. C., Trainor, R. F., et al. 2012, ApJ, 750, 67
Savage, B. D., Sembach, K. R., Tripp, T. M., & Richter, P. 2002, ApJ, 564, 631
Savage, B. D., Sembach, K. R., Wakker, B. P., et al. 2003, ApJS, 146, 125
Schawinski, K., Urry, C. M., Simmons, B. D., et al. 2014, MNRAS, 440, 889
Schneider, D. P., Hartig, G. F., Jannuzi, B. T., et al. 1993, ApJS, 87, 45
Sembach, K. R., & Savage, B. D. 1992, ApJS, 83, 147
Sembach, K. R., Tripp, T. M., Savage, B. D., & Richter, P. 2004, ApJS, 155, 351
Simard, L., Willmer, C. N. A., Vogt, N. P., et al. 2002, ApJS, 142, 1
Steidel, C. C., Erb, D. K., Shapley, A. E., et al. 2010, ApJ, 717, 289
Steidel, C. C., Kollmeier, J. A., Shapley, A. E., et al. 2002, ApJ, 570, 526
Stewart, K. R., Kaufmann, T., Bullock, J. S., et al. 2011, ApJ, 738, 39
Stocke, J. T., Keeney, B. A., Danforth, C. W., et al. 2013, ApJ, 763, 148
Stocke, J. T., Penton, S. V., Danforth, C. W., et al. 2006, ApJ, 641, 217
Strickland, D. K., Heckman, T. M., Colbert, E. J. M., Hoopes, C. G., & Weaver, K. A. 2004, ApJS, 151, 193
Thom, C., Werk, J. K., Tumlinson, J., et al. 2011, ApJ, 736, 1
Tremonti, C. A., Heckman, T. M., Kauffmann, G., et al. 2004, ApJ, 613, 898
Tripp, T. M., Aracil, B., Bowen, D. V., & Jenkins, E. B. 2006, ApJ, 643, L77
Tripp, T. M., Giroux, M. L., Stocke, J. T., Tumlinson, J., & Oegerle, W. R. 2001, ApJ, 563, 724
Tripp, T. M., Sembach, K. R., Bowen, D. V., et al. 2008, ApJS, 177, 39
Trujillo-Gomez, S., Klypin, A., Colin, P., et al. 2013, ArXiv e-prints
Trujillo-Gomez, S., Klypin, A., Primack, J., Churchill, C. W., & Vander Vliet, J. 2014, MNRAS, in preparation
Trujillo-Gomez, S., Klypin, A., Primack, J., & Romanowsky, A. J. 2011, ApJ, 742, 16
Tumlinson, J., Shull, J. M., Giroux, M. L., & Stocke, J. T. 2005, ApJ, 620, 95
Tumlinson, J., Thom, C., Werk, J. K., et al. 2011, Science, 334, 948
—. 2013, ApJ, 777, 59
van de Voort, F., & Schaye, J. 2012, MNRAS, 423, 2991
van de Voort, F., Schaye, J., Booth, C. M., Haas, M. R., & Dalla Vecchia, C. 2011, MNRAS, 414, 2458
Werk, J. K., Prochaska, J. X., Tumlinson, J., et al. 2014, ArXiv e-prints
Wolf, C., Meisenheimer, K., Rix, H.-W., et al. 2003, A&A, 401, 73

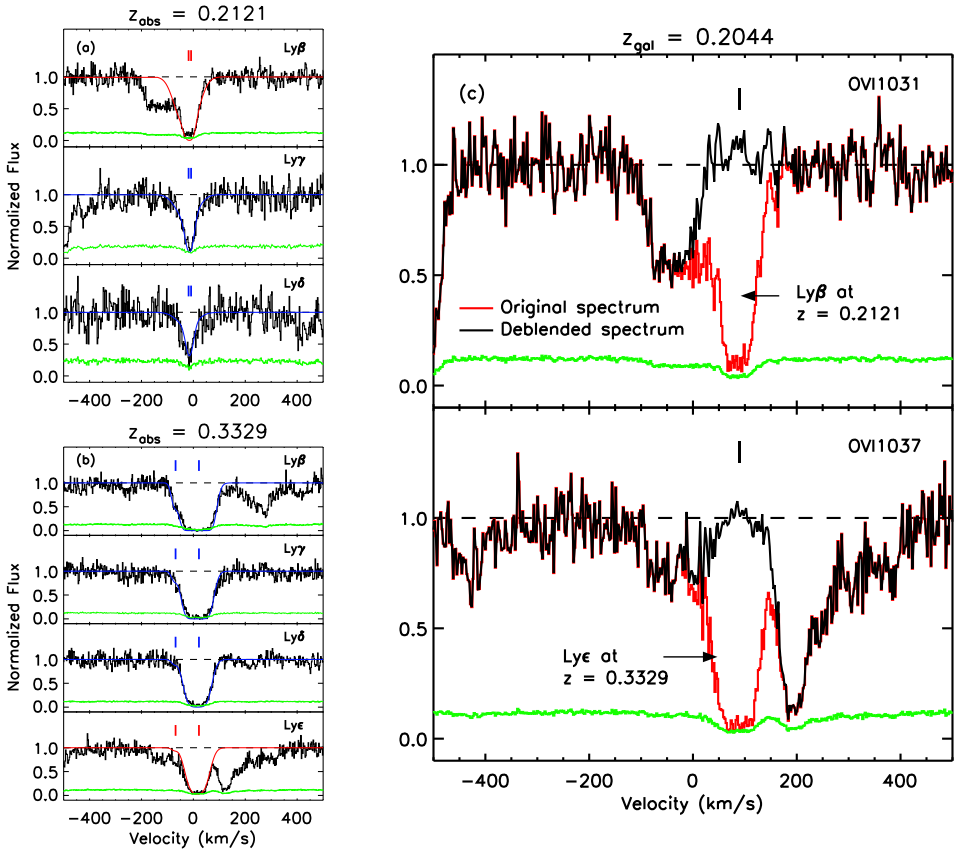

Figure C2. Deblending of O VI $\lambda\lambda$1031, 1037 for absorption associated with the galaxy at z_{gal} = 0.2044 in the field of Q1136−1334. The O VI λ1031 line is blended with Ly β at z_{abs} = 0.2121 and the O VI λ1037 line is blended with Ly ϵ at z_{abs} = 0.3329. The red spectrum is the original raw data and the black spectrum is the result of the deblending process.